

Manuscript version: Author's Accepted Manuscript

The version presented in WRAP is the author's accepted manuscript and may differ from the published version or Version of Record.

Persistent WRAP URL:

<http://wrap.warwick.ac.uk/158272>

How to cite:

Please refer to published version for the most recent bibliographic citation information. If a published version is known of, the repository item page linked to above, will contain details on accessing it.

Copyright and reuse:

The Warwick Research Archive Portal (WRAP) makes this work by researchers of the University of Warwick available open access under the following conditions.

© 2021 Elsevier. Licensed under the Creative Commons Attribution-NonCommercial-NoDerivatives 4.0 International <http://creativecommons.org/licenses/by-nc-nd/4.0/>.



Publisher's statement:

Please refer to the repository item page, publisher's statement section, for further information.

For more information, please contact the WRAP Team at: wrap@warwick.ac.uk.

Quality prediction and rivet/die selection for SPR joints with artificial neural network and genetic algorithm

Huan Zhao^a, Li Han^b, Yunpeng Liu^a and Xianping Liu^{a,*}

^a School of Engineering, University of Warwick, Coventry CV4 7AL, UK

^b Hansher Consulting Ltd., Coventry, UK

* X.Liu@warwick.ac.uk

Abstract

In this study, artificial neural network (ANN) was adopted to predict the quality of SPR joints. Three ANN models were developed respectively for the key joint quality indicators: the interlock, the remaining bottom sheet thickness at the joint center (T_{cen}) and under the rivet tip (T_{tip}). Experimental SPR tests were performed and the results verified the high prediction accuracy of the ANN models. The mean absolute errors (MAE) between the experimental and prediction results for the interlock, T_{cen} and T_{tip} reached 0.058mm, 0.075mm and 0.059mm respectively, and the corresponding mean absolute percentage errors (MAPE) were 14.2%, 22.4% and 10.9%. Moreover, two innovative approaches were proposed to simplify the selection of rivet and die for new joint designs. One was realized by combining the genetic algorithm (GA) with the ANN models, and can generate optimal rivet and die combinations for different joint quality standards. The second was achieved by plotting application range maps of different rivet and die combinations with the help of ANN models, and can quickly select the suitable and accessible rivet and die. Furthermore, interaction effects between different joining parameters on the joint quality were also discussed by analyzing the contour graphs plotted with the ANN models.

Keywords: Self-piercing riveting; Artificial neural network; Genetic algorithm; Rivet and die selection; Application range map; Interaction analysis.

1 Introduction

Self-piercing riveting (SPR), as a mechanical joining process, is suitable to join structures made of similar or dissimilar materials, especially lightweight materials like aluminum alloys [1][2]. It achieved a rapid development in the past two decades due to the strong demands from the automotive industry. Nowadays, the SPR technique has been widely applied to assemble the aluminum alloy body-in-white (BIW) structures [3][4].

For a new SPR joint, it is critical to select suitable rivet and die parameters in order to meet the quality standards. The rivet length, rivet shank diameter, rivet material and rivet hardness level are the four important rivet parameters [5][6][7]. The die type (e.g. Flat die or pip die), die diameter, die depth and pip height are the critical factors for the die selection [8] [9]. In addition to the rivet and die, the effects of the sheet properties,

thickness and sequence on the joint quality should also be considered carefully [10] [11]. For example, Abe et al. [10] reported that the interlock decreased with the increment of bottom steel sheet strength. Ma et al. [11] found that, for the studied sheet thickness, the interlock increased with the increment of the rivet length, but too long rivet resulted in an undesired T_{\min} . A higher joint quality is more likely achieved when the thicker sheet is used as the bottom layer rather than as the top layer [12]. A large number of studies have been carried out, and effectively extended the understandings of the sheet, rivet and die parameters' impact on the SPR joint quality [3]. However, there is not a straightforward way to select the suitable rivet and die for new SPR joints. Till now, the selection of rivet and die still heavily depends on experimental SPR tests designed and assessed by experienced engineers. It would be a great contribution to practical applications if a simpler approach could be developed to facilitate the selection of rivet and die.

To reduce the number of experimental SPR tests during the selection of rivet and die, in last two decades, many finite element analysis (FEA) models have been successfully developed to predict the SPR joint quality. For instance, Mucha [12] successfully developed a two-dimensional (2D) axisymmetric SPR model in MSC Marc Mentat. Carandente et al. [13] established an improved 2D model of SPR process using Simufact.Forming, in which the thermal softening and strain hardening effects on the sheet material strength were considered. Atzeni et al. [14] also established a three-dimensional (3D) simulation model using ABAQUS to predict the SPR joint quality. In addition, a combination of the FEA models and other optimization algorithms was also reported to simplify the selection of rivet and die. For example, through the analysis of variance (ANOVA) using a developed 2D FEA model of clinched joint, Chen et al. [15] successfully selected the suitable reshaping rivet for the clinched joint with 2.0mm+2.0mm AA6061 sheets. This could effectively reduce the dependence on skilled engineers' practical experience during the selection of rivet and die, but a considerable number of FEA simulations are required for each new joint prior to experimental confirmation. Moreover, for general engineers without an in-depth knowledge of FEA and the SPR process, running such simulation models is still a big challenge. Therefore, a much easier quality prediction tool for SPR joints is desirable for practical applications.

Mathematical models can give a straightforward prediction and effectively minimize the above-mentioned disadvantages of FEA models. There are already some mathematical models reported in the public domain to quickly predict the SPR joint quality. Zhao et al. [16] successfully developed multiple regression models to prediction the joint quality of 1.5mm+1.5mm AA5754 sheets with varying rivets and dies. Zhang et al. [17] developed response surface equations to predict the quality of SPR joints with 2.0mm AA5052 top sheet and 2.0mm AA6061 bottom sheet. With the Kriging technique, Tassler et al. [18] established a mathematical model to predict the quality of SPR joints with different sheet thicknesses and yield stresses, rivet lengths and blank-holder forces. The above studies confirmed the effectiveness of mathematic models in SPR joint quality prediction. However, there are two potential challenges during the mathematic model development. The first challenge is that the relationships between the inputs (i.e. joining parameters) and outputs (i.e. joint quality indicators) should be pre-defined in order to select a suitable structure of mathematic model. With the increment of joint design space (i.e. the number and scopes of joining parameters), the variation trends of joint quality indicators will become highly nonlinear. This raises the complexity of relationships between the joining

parameters and quality indicators, and therefore increases the difficulties for the model structure selection. The second challenge is the identification of unknown coefficients during the mathematic model development. The model structure will become increasingly complicated with the increment of joining parameters considered. This will inevitably increase the number of unknown coefficients and therefore increase the difficulties in coefficient identification. For example, Tassler et al. [18] proved the effectiveness of Kriging technique in the joint quality prediction, but also demonstrated the complex procedures to determine all the unknown coefficients in the model. Expert knowledge of optimization algorithms (e.g. genetic algorithm) is required in order to use the Kriging technique.

Different from the mathematic models, artificial neural network (ANN), which has an excellent fitting ability to describe complex relationships between inputs and outputs [19], is much more suitable to develop easy-to-use quality prediction tools. It can involve multiple joining parameters and joint quality indicators, and thus achieve a wider application range. Meanwhile, the development of the prediction tool is straightforward because the ANN can automatically establish the relationships between inputs and outputs by optimizing the weights of connected neurons [20]. To the authors' knowledge, there are few studies relevant to the application of ANN on the SPR joint quality. Fang et al. [21] developed surrogate models of SPR simulation model with the radial basis function (RBF) network, and analyzed the effects of different joining parameters on the joint cross-section dimensions and maximum punch force. Many successful applications of ANN in other industrial fields have been reported in the public domain. For example, Khorasani et al. [22] accurately predicted the average surface roughness (S_a) on laser powder bed fusion process using the multi-layer perceptron ANN. With the back-propagation (BP) neural network, Wang et al. [23] successfully predicted the weld morphology of Al alloy-CFRP welding-rivet hybrid bonding joint. Taking advantages of the FEA model and radial basis function (RBF) neural network, Liu et al. [24] accurately predicted the workpiece deformation induced by the large riveting force during the joining process with a dual-machine-based riveting system. Owing to the powerful self-learning capability and strong robustness, the ANN was introduced in this study to predict the quality of SPR joints.

To further simplify and optimize the selection of rivet and die, genetic algorithm (GA) could be a promising tool in combination with the ANN. The GA is a popular optimization algorithm inspired from the biological evolution process [25]. It is a very powerful tool to deal with the multi-objective optimization problems, and has been widely applied to solve practical optimization issues in different industrial fields. For example, Wang et al. [26] successfully optimized the geometric parameters of the composite honeycomb tip with the help of GA. By combining the response surface methodology (RSM) with the GA, Udayakumar et al. [27] developed a multi-objective optimization method to optimize the process parameters in friction welding process. Zhang et al. [28] also successfully employed the genetic algorithm NSGA-II to optimize the shear strength and peel strength of friction stir spot welding joint. The experiment results verified the effectiveness of the generated Pareto front, and proved the strong capability of GA to deal with multi-objective problems. Considering the multiple quality indicators of SPR joints, the GA together with the ANN was utilized in this study to optimize and simplify the selection of rivet and die.

The main objectives of this study are to develop an easy-to-use quality prediction tool for SPR joints with the

ANN, and to optimize/simplify the selection of rivet and die for new joint design. To overcome the time and financial requirements of experimental SPR tests, a verified FEA model of SPR process was employed to collect the training and testing data for the ANN development. The optimal structures of the ANNs were determined using the trial-and-error method. Laboratory experimental SPR tests were carried out to validate the prediction accuracy of the developed ANNs. The genetic algorithm (GA) was utilized together with the ANNs to automatically select optimal rivets and dies for new sheet combinations. In addition, application range maps for different rivet and die combinations were created using the ANNs to further simplify the rivet and die selection. Contour graphs of joint quality indicators were also plotted with the developed ANNs to address the interaction effects between different joining parameters on the SPR joint quality.

2 Finite element analysis (FEA) model

2.1 Self-piercing riveting process and joint quality evaluation

Fig. 1 illustrates the four steps of the SPR process, including the clamping, piercing, flaring and tools releasing [29]. At the end of the process, the multiple sheets are tightly connected by the mechanical interlock formed between the rivet shank and the bottom sheet. Generally, as shown in **Fig. 2**, the SPR joint quality is assessed by three characteristic indicators measured on the joint cross-sectional profile [30][31], including the rivet head height, the interlock and the minimum remaining bottom sheet thickness (T_{\min}). The rivet head height directly affects the cosmetic appearance of the connected structure and the joint corrosion resistance. Meanwhile, it also influences the final rivet position in the substrates and therefore affects the magnitudes of the interlock and T_{\min} [32]. The interlock is very important for the joint mechanical strengths and failure behaviors. SPR joints with too small interlocks usually have low shearing strengths, and more likely undergo pull-out failures of the rivet shank from the bottom sheet [33]. The T_{\min} is highly associated with the joint corrosion resistance and water-proof performance. Zero or negative T_{\min} would inevitably lead to moisture or water invasion. This would accelerate the corrosion between the steel rivet and aluminum sheets, and cause premature corrosion failure of SPR joints. According to different application requirements, quality standards of the three indicators usually vary from company to company.

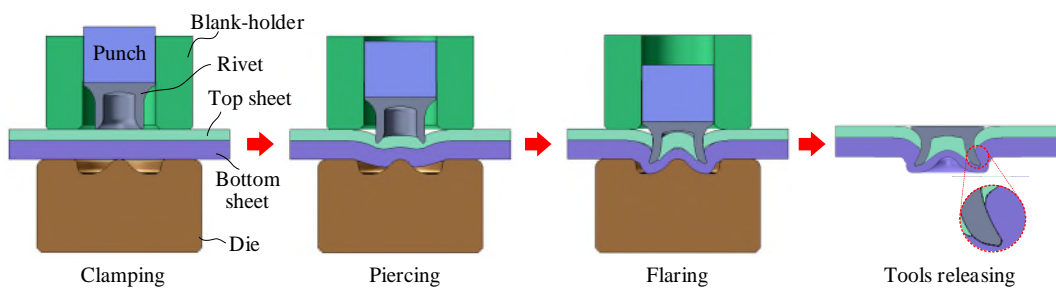


Fig. 1 Schematic of the four steps during the self-piercing riveting process

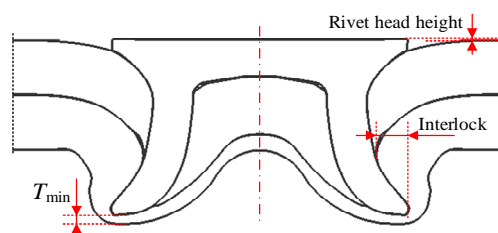


Fig. 2 Joint cross-sectional profile and the three quality characteristic indicators

2.2 Model description

To collect the training and testing data for the ANN development, a previously developed two-dimensional (2D) FEA model of SPR process was adopted. This model was developed using the software Simufact.Forming. As shown in **Fig. 3**, all the freedoms of die were fixed while the sheet edges could move freely during the riveting process. A 5.3kN clamping force (F_1) was applied on the blank-holder to clamp the top and bottom sheets together. The punch had a constant speed ($v_1=300\text{mm/s}$) and moved downward to press the rivet into the sheets. The punch, blank-holder and die were modelled as rigid bodies, while the boron steel rivet and AA5754 sheets were modelled as elastic-plastic bodies. As shown in **Fig. 4**, plastic stress-strain curves were implemented to model the material deformations of the rivet and sheets. The temperature effect on the material properties was only considered for the AA5754. All the deformable parts were meshed using the quad element with four gauss points. The mesh sizes for the rivet, the top sheet and the bottom sheet were set to 0.10mm, 0.10mm and 0.12mm respectively. Automatic element re-meshing was applied to deal with the severe element distortion caused by the large plastic deformations of the top and bottom sheets. A geometric criterion was employed to model the top sheet fracture and the threshold thickness was set to 0.04mm. The Coulomb friction model was adopted and the friction coefficients between different contact parts are given in **Table 1**. More details of the FEA model can be found from the authors' previous study [9].

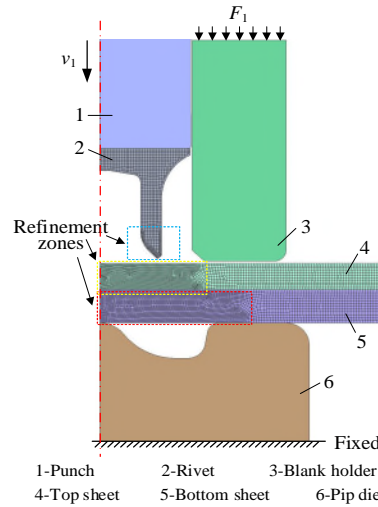


Fig. 3 The two-dimensional FEA model of the self-piercing riveting process

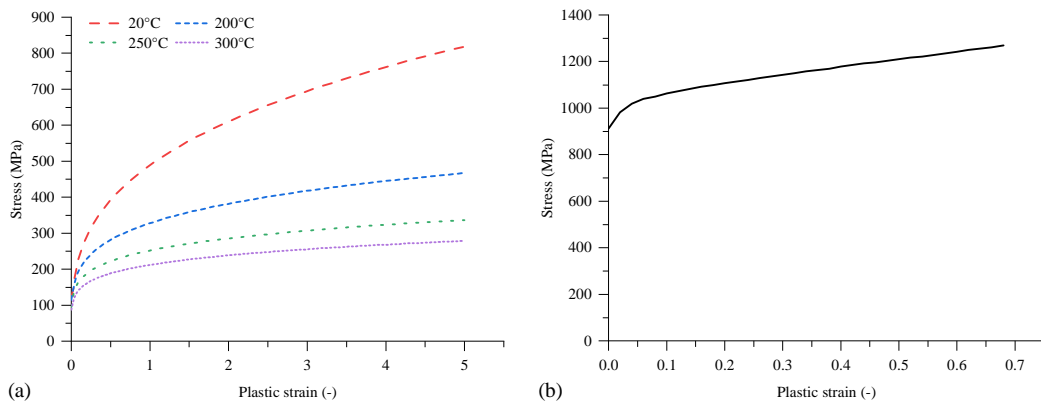


Fig. 4 Plastic stress-strain curves for (a) Aluminum alloy AA5754 (strain rate= 1s^{-1})[13] and (b) Boron steel rivet (20°C , strain rate= 0.01s^{-1}) [9]

Table 1 Friction coefficients used in the FEA model [9]

Contact pairs	Punch-Rivet	Blankholder-sheets	Rivet-Sheets	Top sheet-Bottom sheet	Bottom sheet-Die	Others
Friction coefficients	0.10	0.10	0.10	0.10	0.22	0.10

2.3 Model validation

Before using the FEA model to collect training and testing data for ANN, the prediction accuracy of the developed FEA model was verified again via laboratory experimental SPR tests. As listed in **Table 2**, twenty SPR joints with different configurations were manufactured experimentally. **Fig. 5** illustrates the cross-sectional profiles of the sheets, the semi-tubular rivet and the pip die used in the experiments. The aluminum alloy AA5754 sheets and boron steel rivets were used throughout the experiments. The rivets and dies were supplied by the Tucker GmbH, and the AA5754 sheets were provided by Jaguar Land Rover (JLR). The rivet diameter, rivet hardness and die pip height were fixed at 5.3mm, H0 ($280\pm 30\text{HV}10$) and 0.0mm respectively. Different top sheet thicknesses (T_1), bottom sheet thicknesses (T_2), rivet lengths (L_1), die diameters (D_1) and die depths (H_1) were used to enhance the performance evaluation of the FEA model. Three repetitions were made for each joint configuration using the Tucker servo SPR system shown in **Fig. 6**. The punch speed and the clamping force were the same as that used in the FEA model.

All the specimens were sectioned along the central plane of the rivet, and the joint cross-sectional profiles were captured using an optical microscope. Then, the three quality indicators (i.e. the rivet head height, the interlock and the T_{\min}) were measured on the joint cross-sectional profiles. The mean values of these indicators from the three repetitions were calculated for each joint configuration, as listed in **Table 2**. All the 20 SPR joints were also simulated using the developed FEA model. For easier comparison between the experimental and simulation results, the mean value of the experimentally measured rivet head height for each SPR joint was implemented as the termination criterion of the corresponding SPR simulation. The simulated three quality indicators for each joint were also extracted as listed in **Table 2**.

Table 2 Experiment design and results for the validation of FEA model

Joint configurations					Experimental and simulation results					
Joint no.	Stack /mm (AA5754)	Rivet length L_1 /mm	Die		Rivet head height/mm		Interlock/mm		T_{\min} /mm	
			Diameter D_1 /mm	Depth H_1 /mm	Tested (Mean)	Simulated	Tested (Mean)	Simulated	Tested (Mean)	Simulated
E-1	1.0+1.5	5.0	10.0	1.8	0.03	-0.03	0.44	0.43	0.32	0.22
E-2	1.0+1.5	5.0	9.0	1.6	0.02	0.02	0.60	0.59	0.28	0.17
E-3	1.0+2.0	5.0	9.0	1.6	-0.09	0.01	0.76	0.64	0.51	0.43
E-4	1.5+1.0	5.0	10.0	1.8	-0.19	-0.01	0.16	0.12	0.36	0.23
E-5	1.5+1.0	5.0	9.0	1.6	-0.08	0.03	0.31	0.30	0.23	0.19
E-6	1.5+1.0	6.0	10.0	1.8	0.01	0.00	0.59	0.40	0.13	0.07
E-7	1.5+1.0	6.0	9.0	1.6	-0.08	0.10	0.74	0.68	0.1	0.18
E-8	1.5+1.5	5.0	10.0	2.0	-0.05	0.02	0.25	0.20	0.37	0.34
E-9	1.5+1.5	5.0	10.0	1.8	-0.07	0.01	0.33	0.27	0.48	0.43

E-10	1.5+1.5	5.0	9.0	1.6	0.02	0.03	0.42	0.39	0.53	0.48
E-11	1.5+1.5	5.0	8.0	2.0	-0.04	0.02	0.35	0.34	0.38	0.23
E-12	1.5+1.5	6.0	10.0	1.8	0.04	0.00	0.69	0.57	0.32	0.28
E-13	1.5+1.5	6.0	9.0	1.6	0.01	0.07	0.77	0.73	0.41	0.31
E-14	1.5+2.0	5.0	9.0	1.6	-0.06	0.03	0.56	0.46	0.72	0.70
E-15	1.5+2.0	6.0	10.0	1.8	-0.1	0.00	0.76	0.72	0.56	0.57
E-16	1.5+2.0	6.0	9.0	1.6	-0.12	0.06	0.93	0.76	0.43	0.62
E-17	2.0+1.5	6.0	10.0	1.8	-0.13	0.02	0.43	0.40	0.37	0.21
E-18	2.0+1.5	6.0	9.0	1.6	-0.11	0.05	0.61	0.56	0.22	0.25
E-19	1.8+2.0	6.0	9.0	1.6	0.06	0.01	0.71	0.64	0.39	0.55
E-20	2.0+2.0	6.0	9.0	1.6	0.02	0.04	0.65	0.58	0.37	0.37

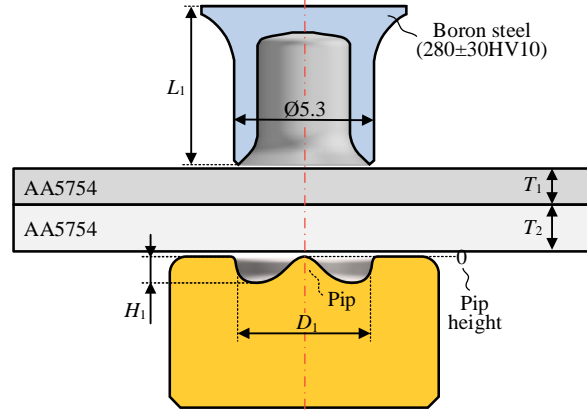


Fig. 5 Cross-sectional profiles of the top sheet, bottom sheet, the semi-tubular rivet and the pip die

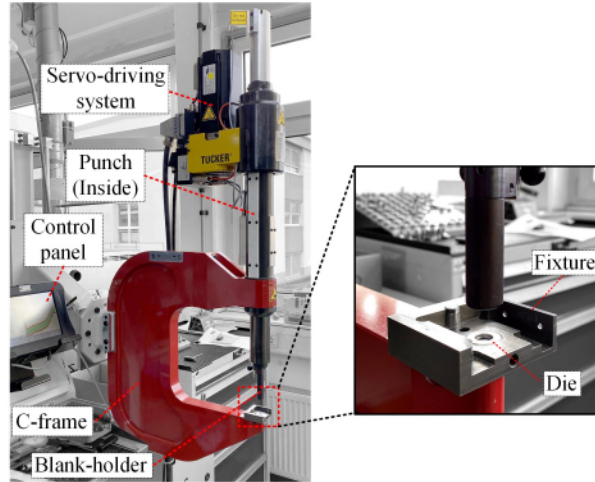


Fig. 6 Structure of the Tucker SPR system

Fig. 7 shows the comparisons of joint cross-sectional profiles extracted from the experimental SPR tests and FEA simulations. By visual observation, a reasonable agreement was found between the simulation and experimental results. The simulated shapes of the deformed rivet and sheets matched well with the experimentally tested ones. Comparisons between the tested and simulated interlock and T_{\min} are given in **Fig. 8**. The calculated mean absolute error (MAE) for the interlock and the T_{\min} were 0.064mm and 0.079mm respectively, and the corresponding Pearson's correlation coefficient (r) were 0.97 and 0.84. These results verified the high prediction accuracy of the FEA model for the interlock and the T_{\min} under various joint configurations. Therefore, the FEA simulation model was used to collect training and testing data for the ANN development.

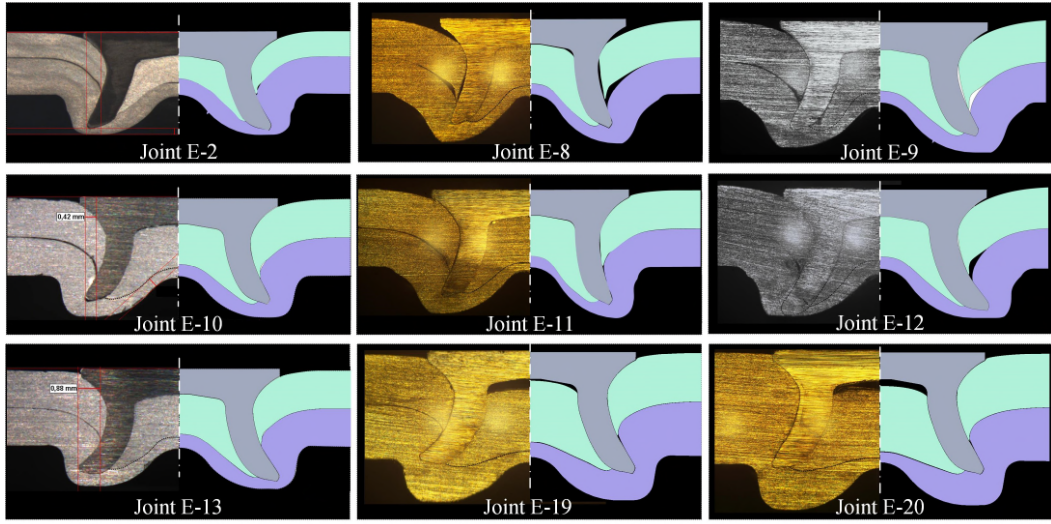


Fig. 7 Comparisons of the joint cross-sectional profiles from the experimental tests and the FEA simulations

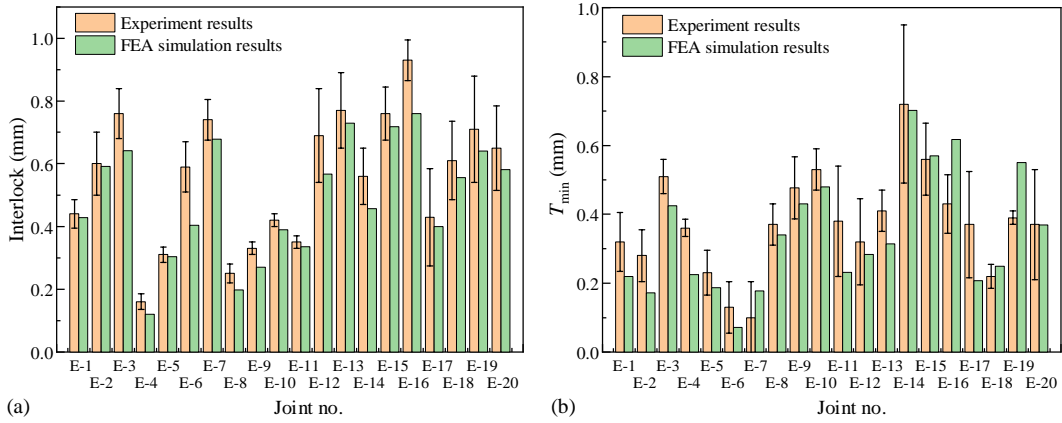


Fig. 8 Comparisons of the experimentally tested and FEA simulated (a) interlock and (b) T_{\min}

3 Development of ANN prediction models

3.1 ANN model architecture

The artificial neural network (ANN) has very powerful self-learning ability, strong robustness and high fault tolerance. It is suitable to describe the complex nonlinear relationships between the inputs and outputs [34] of the SPR process. Compared with the mathematic prediction models (e.g. Kriging technique), the development process of an ANN is much more straightforward and faster because the ANN can automatically learn the highly nonlinear relationships between the multiple joining parameters and quality indicators. The ANN model employed in this study is classified to the feedforward neural network. The back-propagation algorithm was utilized to optimize the internal weights and biases in the ANN models. As shown in **Fig. 9**, it consists of one input layer, one hidden layer and one output layer. The five joint parameters, including the top sheet thickness (T_1), bottom sheet thickness (T_2), rivet length (L_1), die diameter (D_1) and die depth (H_1), were designed as the inputs of neural network. To improve the prediction accuracy and to reduce the difficulty of model training, only one of the joint quality indicators (i.e. interlock, T_{cen} or T_{tip}) was selected as the output. There is also one bias neuron in the input and hidden layer respectively. The neurons in each layer are connected to all neurons in the adjacent layer. The weight ($W_{x,y}^{(i)}$) assigned to each connection indicates the intensity of the signal

transmission between the connected neurons [35]. In the $W_{x,y}^{(i)}$, the x and y denote the numbers of the two connected neurons in the later layer and in the previous layer respectively, and the i denotes the layer number in the ANN. The **activation functions** are the ‘*tansig*’ for the hidden layer and the ‘*purelin*’ for the output layer. The ANN model was established and trained using the software MATLAB R2020a.

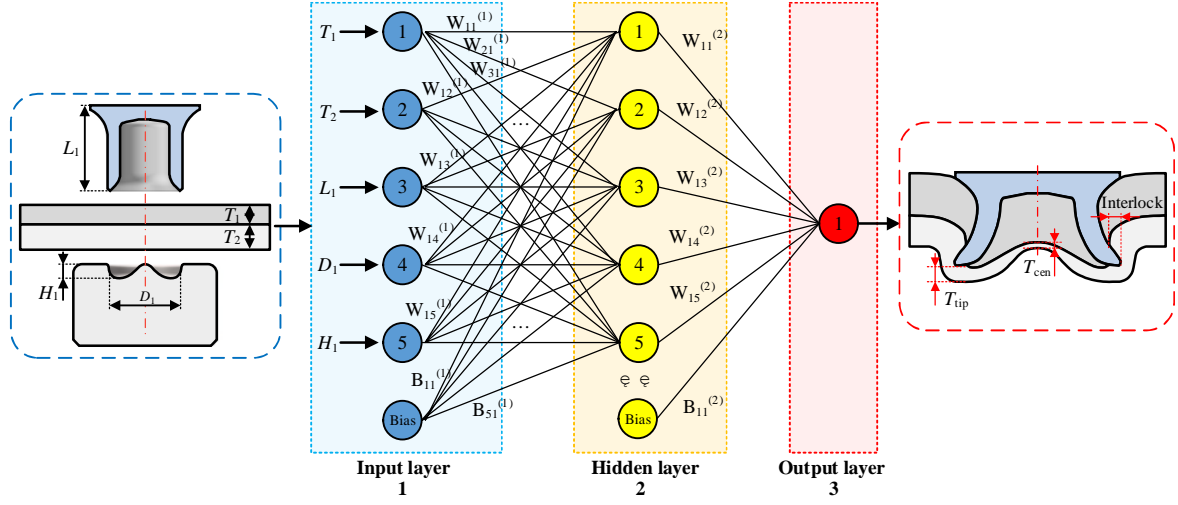


Fig. 9 Structure of the three-layer artificial neural network (ANN)

3.2 Training and testing data acquisition

In this study, the five critical process parameters (T_1 , T_2 , L_1 , D_1 and H_1) were involved in the ANN prediction models. To collect enough training and testing data for the development of ANN models, the full factorial design (3^5) with five parameters and three levels was adopted as listed in **Table 3**. The aluminum alloy AA5754 sheets and boron steel rivets were used. The rivet diameter, rivet hardness and die pip height were also fixed at 5.3mm, H0 and 0.0mm respectively. The rivet head height directly links with the final position of the rivet inserted into the sheets and thus affects the final values of the interlock and T_{\min} [32]. For consistency, a uniform rivet head height (i.e. 0.0mm) was set for all SPR joints by controlling the rivet displacement. A total of 243 joints with different configurations were simulated using the verified FEA model.

Table 3 Full factorial design with five joint parameters and three levels (3^5)

Level	Top sheet thickness T_1/mm	Bottom sheet thickness T_2/mm	Rivet length L_1/mm	Die diameter D_1/mm	Die depth H_1/mm
1	1.0	1.0	5.0	8.0	1.6
2	1.5	1.5	5.5	9.0	1.8
3	2.0	2.0	6.0	10.0	2.0

After all of the simulations were completed, the joint quality indicators of the 243 joints were measured on the simulated joint cross-sectional profiles. The interlock is always formed around the rivet tip and thus relatively easy to measure. In contrast, the formation position of the T_{\min} is not fixed but changes under different joint configurations. **Fig. 10** illustrates four potential positions that the T_{\min} may appear. Because of the uncertain position of the T_{\min} , it is very difficult to establish a single ANN model to predict the T_{\min} directly. By analyzing formation positions of the T_{\min} in the 243 joints, it was found that the T_{\min} had a higher possibility to locate at the joint center (Position 1 in **Fig. 10(a)**) or under the rivet tip (Position 3 in **Fig. 10(c)**). Therefore, in this

study, the remaining bottom sheet thickness at the joint center (T_{cen}) and under the rivet tip (T_{tip}) in each SPR joint were measured for the ANN model development. To keep data consistency, the T_{cen} and the T_{tip} were always measured along the vertical direction. All of the interlock, T_{cen} and T_{tip} values in the 243 joints were recorded as the training and testing data to develop the ANN models.

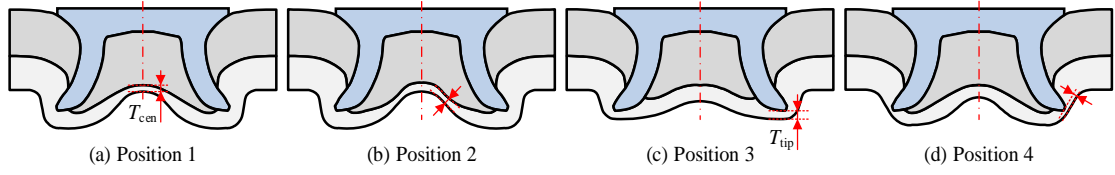


Fig. 10 Potential positions of the minimum remaining bottom sheet thickness (T_{min}) in SPR joints

To eliminate the influences of scope difference between the input parameters, all the five inputs of the 243 SPR joints were normalized using the z-score method (Eq.(1)). All the outputs were calculated with the min-max normalization into the range 0~1 using the Eq.(2). During the training of ANN, the learning rate was set to 0.001 to ensure a high probability of global convergence and a maximum of 5000 iterations was selected to determine the weights.

$$x_{norm} = \frac{x_{input} - \mu}{\sigma} \quad (1)$$

where x_{norm} is the standardized input value, x_{input} is the original input value, μ and σ are the mean and the standard deviation of all input values.

$$y_{norm} = \frac{y_{output} - y_{min}}{y_{max} - y_{min}} \quad (2)$$

where y_{norm} is the normalized output value, y_{output} is the original output value, y_{min} and y_{max} are the minimum and maximum values among all the output values.

3.3 ANN for the interlock

The trial-and-error method was applied to select the appropriate number of hidden layer neurons (N_h). **Fig. 11** illustrates the procedures to determine the optimal ANN for the interlock. First, the ANN with three hidden layer neurons ($N_h=3$) was set up. The 243 SPR joints were divided randomly into training data (70%) and testing data (30%) in each circle. The training and testing stages for the neural network were carried out, and the performance indexes of this developed ANN were calculated and recorded, including the mean absolute error (MAE) in Eq.(3) and the correlation coefficient (r) in Eq.(4) between the FEA simulated and ANN predicted values. The smaller MAE value, the more accurate of the developed ANN model. The closer the r value is to 1, the more relevant the predicted and actual results are. To eliminate the influences of data partitioning and the weights initialization on the performance of ANN, the above developing steps were repeated 20 times. The mean values of all the recorded MAE and r were calculated to evaluate the performance of the current ANN. Seven ANN models with 3~9 neurons in the hidden layer were individually trained and tested. Finally, the performances of these ANNs were compared to choose the optimal one.

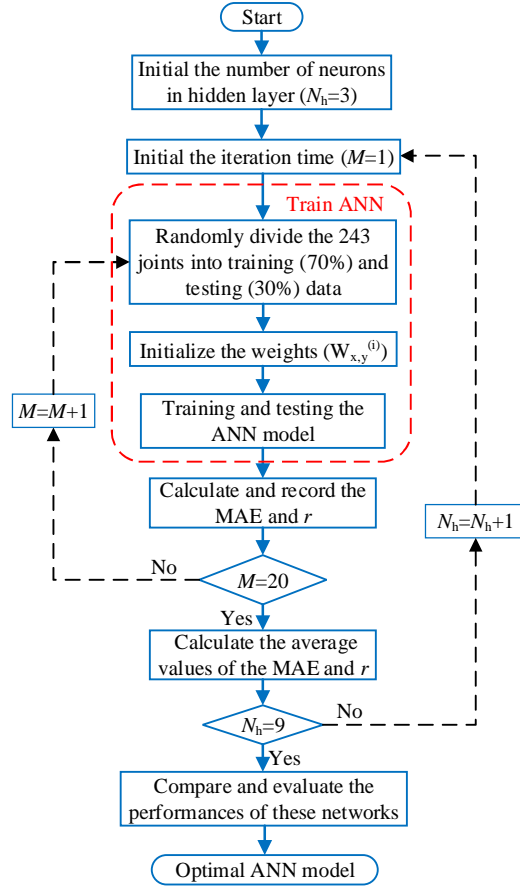


Fig. 11 The algorithm flow chart to select the optimal ANN model for the interlock

$$MAE = \frac{\sum_{j=1}^n |y_{j,s} - y_{j,p}|}{n} \quad (3)$$

where the $y_{j,s}$ and $y_{j,p}$ denote the simulated value by the FEA model and the predicted value by the ANN model of the j th SPR joint. The n is the total number of the SPR joints.

$$r = \frac{\sum Y_s Y_p - \frac{\sum Y_s \sum Y_p}{n}}{\sqrt{(\sum Y_s^2 - \frac{(\sum Y_s)^2}{n})(\sum Y_p^2 - \frac{(\sum Y_p)^2}{n})}} \quad (4)$$

where the \mathbf{Y}_s and \mathbf{Y}_p are the matrixes of the FEA simulation results and the predicted results from the ANN model separately. The n is the total number of the SPR joints.

The values of MAE and r for the seven ANNs are compared in **Fig. 12**. For the training data, it can be seen that the value of MAE rapidly decreased and the corresponding value of r gradually increased when the number of hidden layer neurons (N_h) increased from 3 to 9. However, for the testing data, the MAE value firstly decreased but then increased, whilst the corresponding r value firstly increased and then decreased with the increment of the N_h . The smallest MAE and the largest r were observed in the ANN with 5 hidden layer neurons. This indicated that the ANN with 5 hidden layer neurons had the best fitting degree. The performance degradation of the ANNs with the N_h greater than 5 might attributed to the over-fitting problem. Therefore, the

ANN with 5 hidden layer neurons was selected as the optimal one for the interlock. Comparisons between the FEA simulated and the ANN predicted interlock values are shown in **Fig. 13**. Good correlations were found for both of the training and testing data. The mean values of MAE for the training and testing data were 0.017mm and 0.023mm respectively, and the corresponding average correlation coefficient (r) were 0.994 and 0.990. Therefore, the optimized ANN for the interlock demonstrated a very high prediction accuracy.

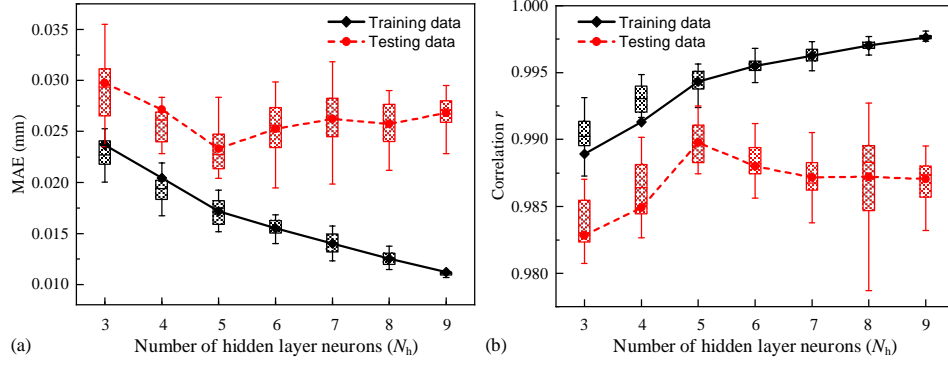


Fig. 12 The performances of ANNs with different numbers of hidden layer neurons (N_h) for the interlock: (a) MAE and (b) correlation coefficient (r)

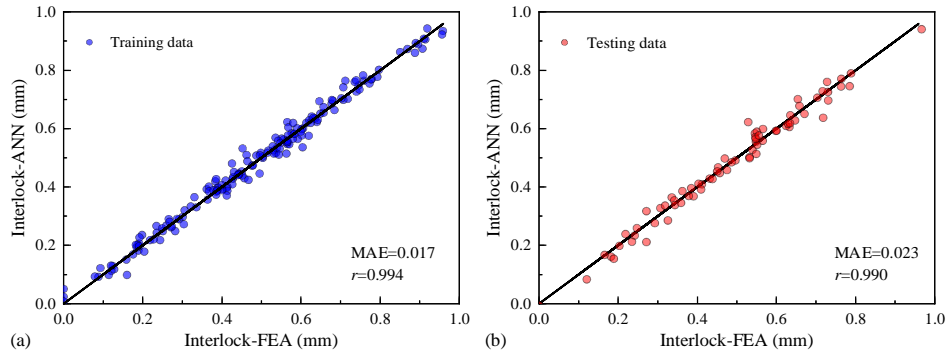


Fig. 13 Comparisons between the ANN predicted and the FEA simulated interlock values: (a) Training data and (b) Testing data

3.4 ANNs for the T_{cen} and T_{tip}

Similar procedures, as the optimal ANN selection for the interlock illustrated in **Fig. 11**, were also carried out to determine the optimal structures of ANNs for the T_{cen} and T_{tip} . The performances of nine ANNs for the T_{cen} with different hidden layer neurons ($N_h=3 \sim 11$) are presented in **Fig. 14**. It can be seen that the ANN with 8 hidden layer neurons achieved the smallest MAE and the second largest r for the testing data, and thus was selected as the optimal ANN for the T_{cen} . Comparisons between the FEA simulated and the optimal ANN predicted T_{cen} in **Fig. 15** indicated the good correlations for the training and testing data. The mean values of MAE for the training and testing data were 0.011mm and 0.022mm respectively, and the corresponding average values of r reached up to 0.998 and 0.992. According to the performances of the nine ANNs for the T_{tip} shown in **Fig. 16**, the ANN with 7 hidden layer neurons was chosen as the optimal one. **Fig. 17** also demonstrates the good correlations between the FEA simulated and the optimal ANN predicted T_{tip} for the training and testing data. The mean values of MAE were 0.018mm and 0.033mm respectively for the training and testing data, and the average values of r reached 0.998 and 0.994. Thus, the optimal ANNs for the T_{cen} and T_{tip} also achieved high prediction accuracies for SPR joints within the studied ranges.

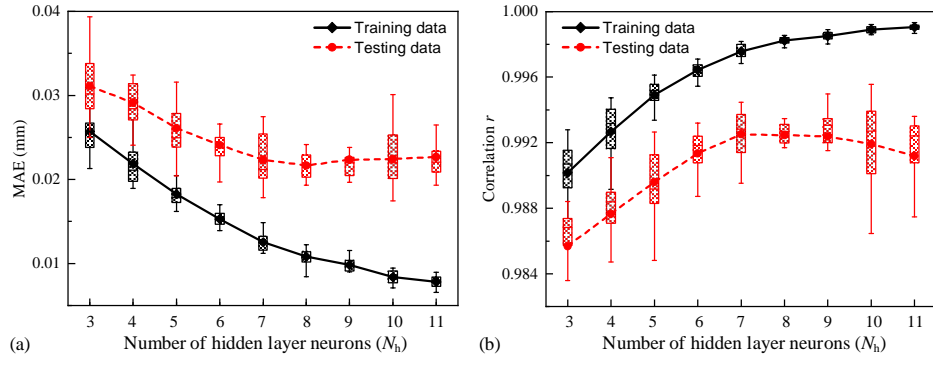


Fig. 14 The performances of ANNs with different numbers of hidden layer neurons (N_h) for the T_{cen} : (a) MAE and (b) correlation coefficient (r)

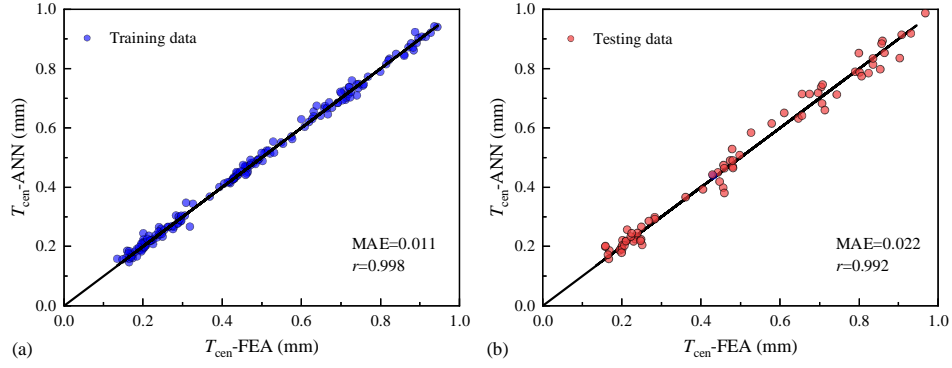


Fig. 15 Comparison between the ANN predicted and the FEA simulated T_{cen} values: (a) Training data and (b) Testing data

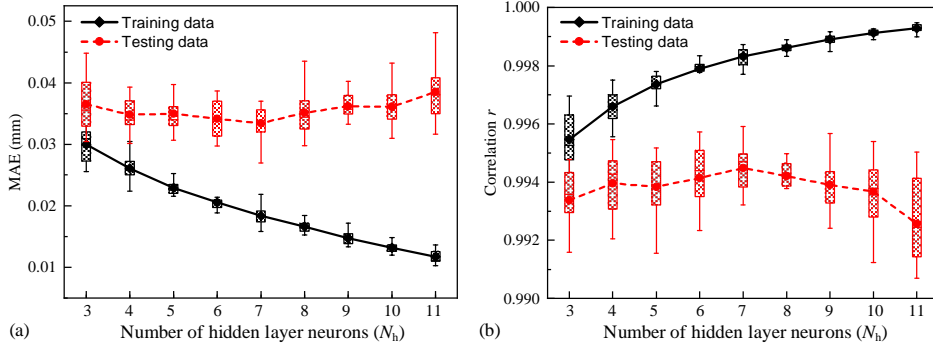


Fig. 16 The performances of ANNs with different numbers of hidden layer neurons (N_h) for the T_{tip} : (a) MAE and (b) correlation coefficient (r)

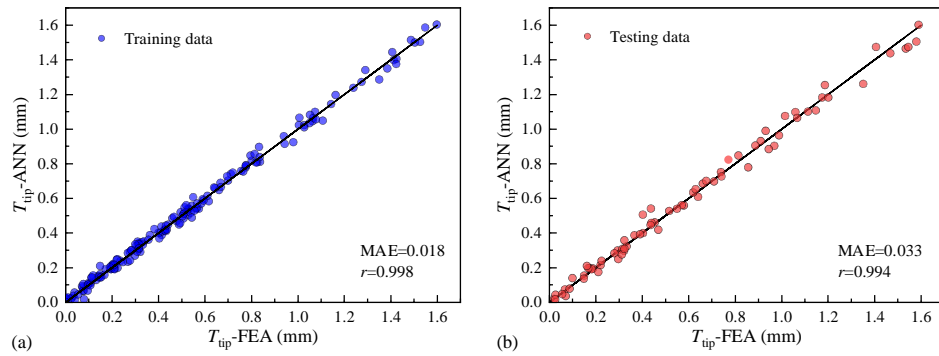


Fig. 17 Comparison between the ANN predicted and the FEA simulated T_{tip} values: (a) Training data and (b) Testing data

3.5 Validation of the ANN models

To validate the prediction accuracy of the developed ANNs, another 23 new SPR joints with different configurations, as listed in **Table 4**, were experimentally fabricated using the Tucker servo SPR system shown in **Fig. 6**. All of the experimental conditions were the same as that used in the validation tests for the FEA model. Three repetitions were performed for each joint configuration, and the mean values of the interlock, the T_{cen} and the T_{tip} were recorded in **Table 4**. Moreover, the three quality indicators of the 23 joints were also predicted with the FEA model and the developed ANNs, as shown in **Table 4**. For easier comparisons, the joint quality data in **Table 4** are also plotted in line graphs as shown in **Fig. 18** and **Fig. 19**.

Comparisons between the interlock values from the experimental tests, the FEA model and the developed ANN are presented in **Fig. 18**. It can be seen that the changing trends of the interlock were almost the same on the three curves. The interlock predicted by the ANN agreed well with that from the experimental tests in 20 out of the 23 SPR joints, except for the joints E-23, E-34 and E-36. The MAE, mean absolute percentage error (MAPE) and r between the experimentally tested and ANN predicted interlocks were 0.058mm, 14.2% and 0.978 respectively. In SPR joints with relatively small interlocks, such as in E-26 and E-42, the small absolute errors (0.04mm, 0.03mm) between the tested and the ANN predicted interlocks still led to large absolute percentage errors (22.2%, 23.1%). This directly caused the relatively large MAPE for the interlock (i.e. 14.2%). Considering the magnitudes of the MAE and r , it can be concluded that the developed ANN for the interlock could give an accurate prediction result for SPR joints within the studied ranges. In addition, the interlock values predicted by the ANN were quite consistent with that predicted by the FEA model. The calculated MAE, MAPE and r values between the ANN predicted and FEA simulated interlock values were 0.039mm, 9.7% and 0.994. This means that the prediction accuracy of the ANN reached almost the same accuracy level as the FEA model.

Fig. 19(a) shows the values of the T_{cen} from the ANN, FEA model and experimental tests. It can be seen that, in the majority of the 23 SPR joints, the changing trend and magnitudes of the T_{cen} predicted by the ANN showed reasonable agreements with that from the experimental tests. The corresponding MAE, MAPE and r values were 0.075mm, 22.4% and 0.881 respectively. The joint E-23 was excluded when calculating the MAPE because the absolute percentage error in this joint was extremely large (800%). The predicted T_{cen} from the FEA model and the ANN were almost the same for all joints, and the calculated MAE, MAPE and r values were 0.033mm, 7.5% and 0.978 respectively. This means that the prediction accuracy of the ANN for T_{cen} also reached almost the same level as the FEA model.

Fig. 19(b) illustrates the values of the T_{tip} obtained from the experimental tests, the FEA model and the ANN. It can be seen that the developed ANN not only successfully predicted the changing trend of the T_{tip} but also accurately predicted the magnitudes of the T_{tip} in almost all of the 23 SPR joints. The calculated MAE, MAPE and r values for T_{tip} between the experimental tested and the ANN predicted results were 0.059mm, 10.9% and 0.996 respectively. These indicate that the developed ANN is capable of accurately predicting the T_{tip} within the studied ranges. Moreover, The MAE, MAPE and r values between the predicted T_{tip} from the FEA model and the ANN were 0.038mm, 7.0% and 0.993 respectively. This means that the prediction accuracy of the

ANN for T_{tip} is also as high as that of the FEA model. Based on the above results, it is reasonable to conclude that the developed ANNs for the interlock, the T_{cen} and the T_{tip} reached the same prediction accuracy levels as the FEA model, and can be used to predict the SPR joint quality within the defined parameter ranges.

Table 4 Experiment design and results for the validation of ANNs

Joint configurations					Experiment, prediction and simulation results								
Joint no.	Stack /mm (AA5754)	Rivet length L_i /mm	Die		Interlock/mm			T_{cen} /mm			T_{tip} /mm		
			Diameter D_i /mm	Depth H_i /mm	Predicted (ANN)	Simulated (FEA)	Tested (Mean)	Predicted (ANN)	Simulated (FEA)	Tested (Mean)	Predicted (ANN)	Simulated (FEA)	Tested (Mean)
E-21	1.0+1.8	5.0	8.0	2.0	0.53	0.58	0.59	0.71	0.66	0.70	0.33	0.35	0.39
E-22	1.5+1.8				0.38	0.37	0.41	0.54	0.56	0.22	0.85	0.75	0.90
E-23	2.0+1.8				0.19	0.18	0.30	0.18	0.16	0.02	1.42	1.24	1.51
E-24	1.0+1.8		10.0	2.0	0.46	0.51	0.49	0.73	0.70	0.76	0.37	0.38	0.47
E-25	1.5+1.8				0.29	0.31	0.33	0.59	0.57	0.50	0.89	0.80	0.93
E-26	2.0+1.8				0.14	0.19	0.18	0.16	0.18	0.11	1.39	1.40	1.54
E-27	1.2+1.0	5.0	8.0	2.0	0.49	0.50	0.48	0.29	0.34	0.33	0.10	0.14	0.12
E-28	1.2+1.5				0.48	0.52	0.51	0.52	0.56	0.35	0.29	0.32	0.34
E-29	1.2+2.0				0.48	0.55	0.52	0.7	0.72	0.62	0.71	0.73	0.80
E-30	1.2+1.0		10.0	2.0	0.20	0.23	0.16	0.27	0.32	0.41	0.25	0.24	0.27
E-31	1.2+1.5				0.33	0.36	0.34	0.54	0.51	0.56	0.35	0.37	0.41
E-32	1.2+2.0				0.42	0.46	0.49	0.71	0.72	0.68	0.76	0.71	0.83
E-33	1.2+1.8	5.0	8.0	2.0	0.47	0.51	0.53	0.63	0.64	0.55	0.50	0.50	0.57
E-34	1.2+1.8	6.0			0.68	0.73	0.86	0.67	0.75	0.67	0.28	0.33	0.36
E-35	1.2+1.8	5.0	10.0	2.0	0.39	0.44	0.47	0.65	0.63	0.66	0.57	0.55	0.63
E-36	1.2+1.8	6.0			0.76	0.84	0.90	0.71	0.69	0.71	0.23	0.24	0.29
E-37	1.2+1.8	5.0	9.0	1.6	0.53	0.60	0.59	0.7	0.61	0.73	0.44	0.46	0.47
E-38	1.2+1.8		10.0	1.8	0.42	0.47	0.48	0.67	0.63	0.65	0.49	0.51	0.48
E-39	1.2+1.2	5.0	10.0	1.8	0.28	0.32	0.36	0.39	0.40	0.49	0.28	0.29	0.24
E-40	1.2+1.8				0.42	0.47	0.47	0.67	0.63	0.64	0.49	0.51	0.50
E-41	1.5+1.5				0.27	0.27	0.33	0.45	0.43	0.48	0.54	0.56	0.63
E-42	1.8+1.2				0.10	0.13	0.13	0.25	0.21	0.19	0.62	0.63	0.63
E-43	1.8+1.8				0.23	0.25	0.26	0.44	0.40	0.21	1.16	1.04	1.26

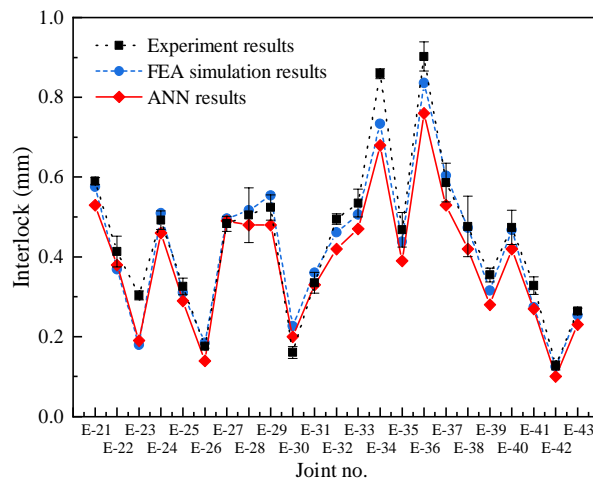


Fig. 18 Comparisons of the interlock from the experimental tests, FEA simulation model and the ANN

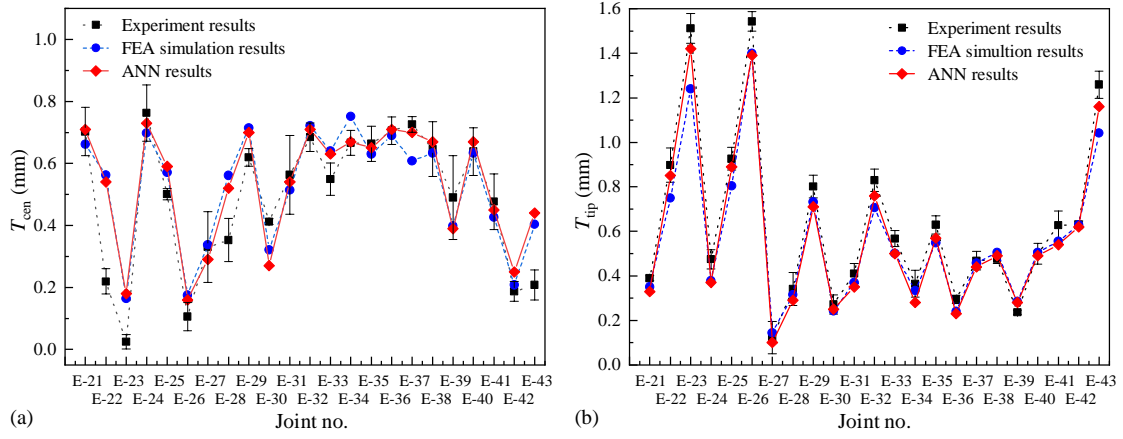


Fig. 19 Comparisons of the (a) T_{cen} and (b) T_{tip} from the experimental tests, the FEA model and the ANNs

3.6 Graphical user interface (GUI)

For the convenience of practical applications, a graphical user interface (GUI) integrating the three established ANNs was developed using the App Designer in MATLAB R2020a, as shown in **Fig. 20**. By simply entering the five pre-defined joint parameters, this GUI will call the three ANNs to calculate the interlock, T_{cen} and T_{tip} , and then display the prediction results to the user within seconds. Compared with the experimental SPR test and the FEA model, this GUI is quicker, more user-friendly and more suitable for industry applications.

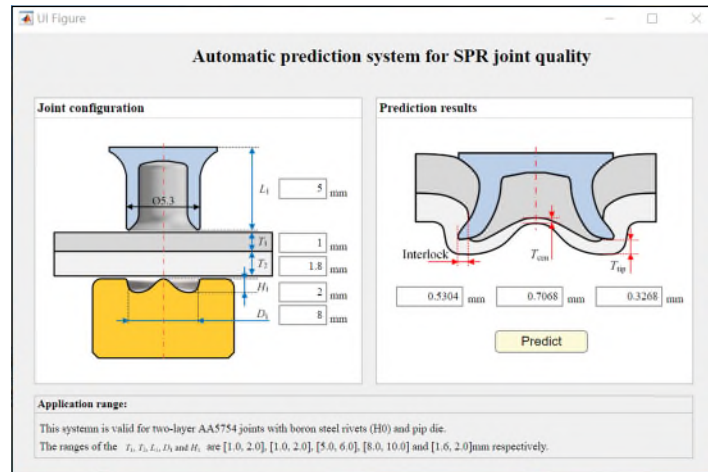


Fig. 20 The graphical user interface (GUI) for the SPR joint quality prediction

4 Genetic algorithm (GA) for the selection of rivet and die

The ANNs are capable to predict the joint quality, but cannot automatically select suitable rivets and dies for a given sheet combination. To reduce the dependence on engineers' experience, the developed ANNs in combination with the genetic algorithm (GA) are used to simplify and optimize the selection of rivet and die. This can be achieved by maximizing the interlock, T_{cen} and T_{tip} . However, because of the contradictory relationships among the three quality indicators, it is impossible to achieve the maximum values of the three quality indicators concurrently [28]. The optimal combination of rivet and die always changes with the variation of the selected joint quality criteria. Therefore, instead of only one optimal solution, in this study, a Pareto optimal solution set of rivet and die combinations was generated using the GA to meet the requirements of different joint quality standards.

4.1 Optimization procedure

The optimization process was carried out using the Global Optimization Toolbox in MATLAB R2020a. The built-in function ‘gamultiobj’, which integrates a controlled elitist genetic algorithm (i.e. a variant of Non-dominated Sorting Genetic Algorithm II (NSGA- II)), was employed to get the Pareto optimal solution set. This controlled elitist GA has a very good exploration performance [28] and can effectively maintain the population diversity [36]. **Fig. 21** illustrates the multi-objective optimization procedures with the GA and the three ANNs. Firstly, the population size was assigned, and the initial population was created. Then, the scores for the population were generated by calculating the objective functions, and were also evaluated to determine whether the termination conditions were met or not. If yes, the optimization iteration was terminated and the Pareto optimal solutions were obtained. Otherwise, the main iteration in function ‘gamultiobj’ was processed, including the selection of parents for next generation, creation of the next generation with mutation and crossover, scoring the children, combining the children to the extended population, trimming the extended population for diversity conservation and forming a new population. The evaluation procedure continued until the stopping criterion was met. The three ANNs for the interlock, T_{cen} and T_{tip} were called to calculate the scores of the population. For a specific sheet combination, the rivet length (L_1), die diameter (D_1) and die depth (H_1) were optimized using the GA by maximizing the three joint quality indicators. **By predefining the scopes of three quality indicators, the GA can directly generate a Pareto optimal solution set satisfying the selected joint quality standard. In this study, to recognize optimal rivet and die combinations complying different quality standards, the variation ranges of the quality indicators were not constrained.**

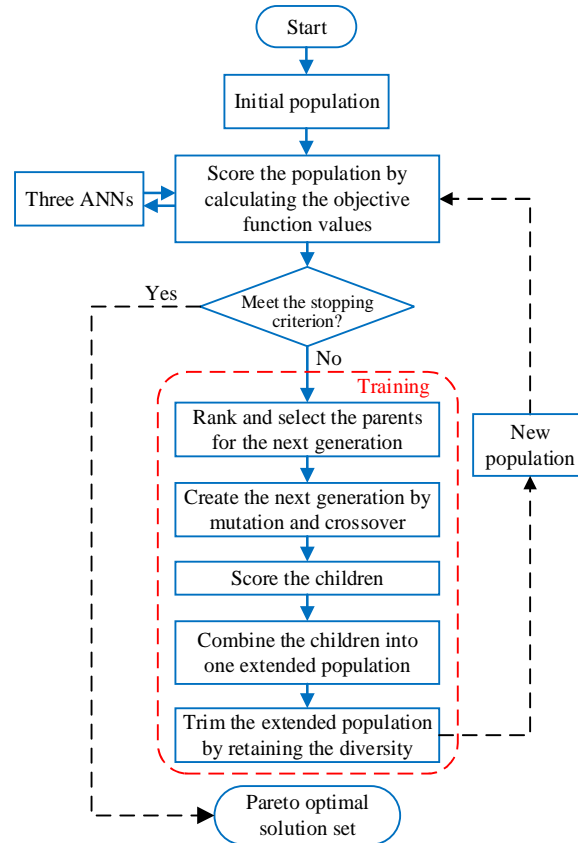


Fig. 21 Flow chart to optimize the rivet and die with the ANNs and genetic algorithm (GA)

As listed in **Table 5**, five different sheet combinations were used to demonstrate the proposed optimization procedures for the selection of rivet and die in practical applications. **Table 6** shows the detailed setting parameters of the GA and the bounds of the L_1 , D_1 and H_1 . The population size was set to 50, and the maximum generation was 500. The crossover and migration rates were 0.80 and 0.20 respectively. The Pareto front population fraction was set to 0.35 to get 18 Pareto optimal solutions for each sheet combination. These Pareto optimal solutions are non-dominated with respect to each other. In other words, when moving from one Pareto solution to another, a certain amount of gain in one objective(s) is always accompanied with a certain amount of sacrifice in the other(s).

Table 5 Five top and bottom sheet combinations

Case No.	Top sheet thickness T_1 /mm (AA5754)	Bottom sheet thickness T_2 /mm (AA5754)
1	1.0	1.0
2	1.0	2.0
3	1.5	1.5
4	2.0	1.0
5	2.0	2.0

Table 6 Setting parameters used in the genetic algorithm

Optimization options	Setting condition
	$5.0 \leq L_1 \leq 6.0$
Rivet and die bounds	$8.0 \leq D_1 \leq 10.0$
	$1.6 \leq H_1 \leq 2.0$
Population size	50
Selection function	Tournament with size 2
Creation function	Feasible population
Crossover fraction	0.80
Mutation function	Adaptive feasible
Crossover function	Scattered
Migration direction	Forward
Migration fraction	0.20
Distance measure function	Distance crowding
Pareto front population fraction	0.35

4.2 Optimization results

For the Case No. 1 (i.e. 1.0mm+1.0mm), the eighteen Pareto optimal solutions are listed in **Table 7**. It can be seen that the interlock, T_{cen} , and T_{tip} reached their maximum values in different Pareto optimal solutions: the maximum interlock (0.89mm) in Solution No.18, the maximum T_{cen} (0.58mm) in Solution No.13 and the maximum T_{tip} (0.21mm) in Solution No.1. To clearly show the changing trends of these quality indicators within the 18 optimal solutions, the joint quality results in **Table 7** were plotted in **Fig. 22(a)**. Obviously opposite changing trends were found between the interlock and the T_{tip} . By optimizing the L_1 , D_1 and H_1 , the interlock increased from 0.30mm to 0.89mm, while the corresponding T_{tip} decreased from 0.21mm to nearly zero. The T_{cen} was less affected by the rivet and die, and just fluctuated within the range of 0.46mm to 0.58mm.

Using the **Fig. 22(a)**, the optimal rivet and die under different quality standards for the 1.0mm+1.0mm sheet combination can be easily identified. For example, according to the standard of a world-leading car manufacturer, the interlock and T_{min} should be greater than 0.4mm and 0.2mm respectively for SPR joints with aluminum alloy bottom sheet [3]. By adding two reference lines (black for the interlock and green for the T_{min})

onto the **Fig. 22(a)**, it can be clearly seen that the 1.0mm+1.0mm sheet combination could not be successfully connected by optimizing the L_1 , D_1 and H_1 within the studied ranges. Further optimization of other rivet and die parameters, such as the rivet diameter, the rivet type and the die type, is required in order to improve the joint quality. However, if reducing the quality standard of the T_{\min} from 0.2mm to 0.1mm (yellow reference line), there would be five Pareto optimal solutions (in Zone1) conforming to the modified quality standard. Considering the importance of the interlock for the joint mechanical strengths, the Solution No.8 with a larger interlock (0.59mm) might be the best solution for the 1.0mm+1.0mm sheet combination.

Table 7 Pareto optimal solution set for Case No.1 (1.0mm+1.0mm)

Solution No.	Sheets /mm	Optimized rivet and die			Joint quality results (ANN)		
		Rivet length L_1 /mm	Die diameter D_1 /mm	Die depth H_1 /mm	Interlock /mm	T_{cen} /mm	T_{tip} /mm
1	1.0+1.0	5.0	10.0	1.6	0.30	0.47	0.21
2	1.0+1.0	5.0	10.0	1.6	0.30	0.47	0.21
3	1.0+1.0	5.0	10.0	1.7	0.30	0.45	0.20
4	1.0+1.0	5.3	9.8	1.6	0.43	0.47	0.17
5	1.0+1.0	5.0	9.5	1.7	0.46	0.44	0.16
6	1.0+1.0	5.2	9.5	1.6	0.51	0.47	0.16
7	1.0+1.0	5.3	9.5	1.6	0.56	0.47	0.14
8	1.0+1.0	5.3	9.5	1.7	0.59	0.46	0.13
9	1.0+1.0	5.3	9.0	1.6	0.61	0.48	0.10
10	1.0+1.0	6.0	10.0	1.7	0.61	0.49	0.08
11	1.0+1.0	6.0	9.8	1.6	0.67	0.51	0.07
12	1.0+1.0	5.9	8.0	1.6	0.70	0.57	0.02
13	1.0+1.0	6.0	8.0	1.6	0.71	0.58	0.01
14	1.0+1.0	6.0	8.0	1.7	0.74	0.53	0.01
15	1.0+1.0	6.0	8.0	1.7	0.76	0.52	0.00
16	1.0+1.0	6.0	8.1	1.7	0.78	0.51	0.00
17	1.0+1.0	6.0	9.5	1.8	0.81	0.49	0.04
18	1.0+1.0	6.0	9.0	1.7	0.89	0.49	0.02

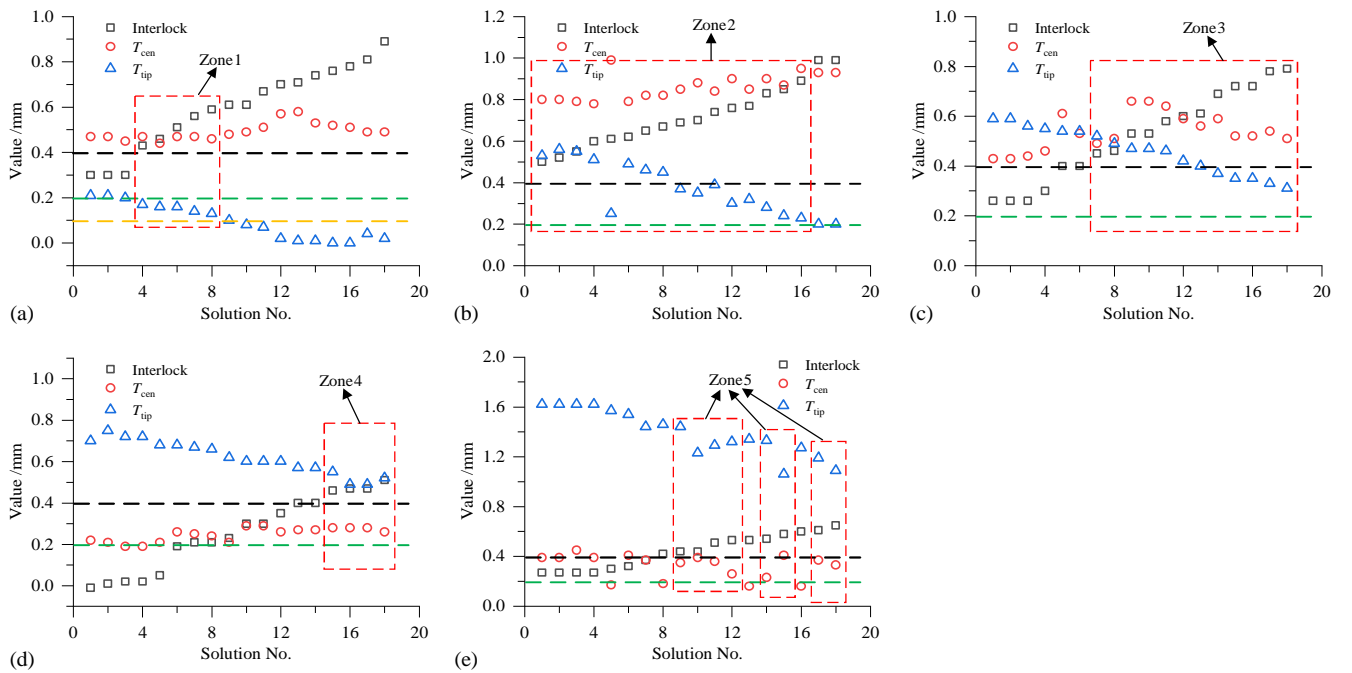


Fig. 22 Changing trends of the interlock, T_{cen} and T_{tip} with the optimized rivet and die: (a) 1.0mm+1.0mm, (b) 1.0mm+2.0mm, (c) 1.5mm+1.5mm, (d) 2.0mm+1.0mm and (e) 2.0mm+2.0mm

The Pareto optimal solutions for other four sheet combinations are also plotted in **Fig. 22(b)(c)(d)(e)** to facilitate the selection of optimal rivet and die. For clarity, the detailed Pareto optimal solutions are not presented in tabular form anymore. It can be seen that the interlock, T_{cen} and T_{tip} in **Fig. 22(b)(c)(d)(e)** demonstrated very similar changing trends to that in **Fig. 22(a)**: the increment of interlock was always accompanied with the rapid decrease of T_{tip} and the fluctuation of T_{cen} within a small range. According to the joint quality standard from [3] (i.e. interlock $> 0.4\text{mm}$ and $T_{min} > 0.2\text{mm}$), all of the four sheet combinations can be successfully connected by optimizing the L_1 , D_1 and H_1 . From the acceptable solutions in Zone2 of **Fig. 22(b)**, the optimized rivet and die in the Solution No.16 might be the best option for the 1.0mm+2.0mm sheet combination. Similarly, the best solutions for the rest three sheet combinations were also easily identified from the acceptable solutions shown in Zone3 of **Fig. 22(c)**, Zone4 of **Fig. 22(d)** and Zone5 of **Fig. 22(e)**: the Solution No.18 for the 1.5mm+1.5mm sheet combination, the Solution No.18 for the 2.0mm+1.0mm sheet combination and the Solution No.18 for the 2.0mm+2.0mm sheet combination.

By comparing the acceptable solution ranges (Zone2, 3 and 4) in **Fig. 22(b)(c)(d)**, it was also found that the sheet combination with a thin top sheet and a thick bottom sheet (e.g. 1.0mm+2.0mm) is more compatible with the rivet and die, and therefore much easier to be successfully connected. In contrast, the sheet combination with a thick top sheet and a thin bottom sheet (e.g. 2.0mm+1.0mm) is more demanding for the rivet and die, and thus more difficult to be connected successfully. This is in a good agreement with the results reported in study [12]. Meanwhile, the T_{min} was more likely formed around the rivet tip in the sheet combination with a thin top sheet and a thick bottom sheet ($T_{tip} < T_{cen}$ in **Fig. 22(b)**), but more likely formed around the joint central area in the sheet combination with a thick top sheet and a thin bottom sheet ($T_{tip} > T_{cen}$ in **Fig. 22(d)**).

Based on the above case studies, it can be concluded that the developed joint quality optimization tool could effectively simplify the selection of rivet and die according to different joint quality standards.

5 Application range map for the selection of rivet and die

In addition to the aforementioned rivet and die selection approach with the ANNs and GA, suitable rivet and die combinations for a new sheet combination can also be quickly identified by plotting application range maps of different rivet and die combinations with the help of developed ANNs. **Fig. 23** shows the four steps to determine such application range map: (a) Select a rivet and die combination; (b) Plot the three contour graphs of interlock, T_{cen} and T_{tip} within the selected thickness ranges of the top and bottom sheets (e.g. 1.0mm~2.0mm) using the developed ANNs; (c) Divide each contour graph into ‘Passed’ and ‘Failed’ regions according to the selected joint quality standard (e.g. interlock $> 0.4\text{mm}$ and $T_{min} > 0.2\text{mm}$); (d) Overlap the three contour graphs together to visualize the suitable (i.e. green region) and unsuitable (i.e. yellow region) application ranges for the selected rivet and die combination.

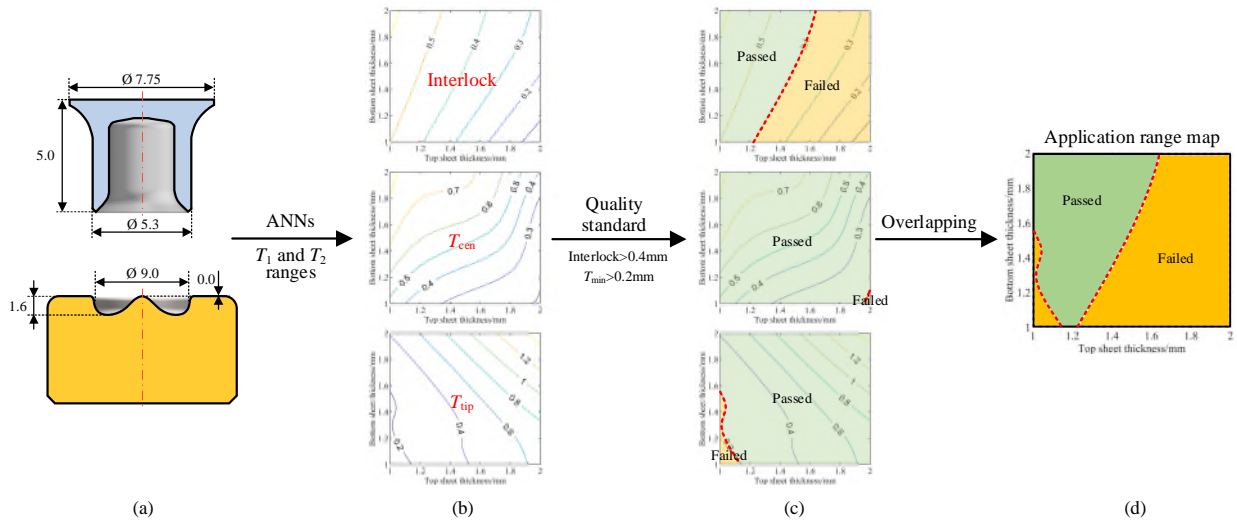


Fig. 23 Four steps to identify the application range map of a specific rivet and die combination

The application range generally varies with different rivet and die combinations. For example, the application ranges of two rivet and die combinations (i.e. Combination 1: $L_1=5.0\text{mm}$, $D_1=9.0\text{mm}$ and $H_1=1.6\text{mm}$; Combination 2: $L_1=6.0\text{mm}$, $D_1=9.0\text{mm}$ and $H_1=1.6\text{mm}$) are plotted in **Fig. 24** following the procedures presented in **Fig. 23**. The sheet thickness range is $1.0\text{mm}\sim 2.0\text{mm}$, and the joint quality standard employed is that the interlock $> 0.4\text{mm}$ and $T_{\min} > 0.2\text{mm}$. It can be seen that the application ranges of the two rivet and die combinations are quite different. As shown in **Fig. 24(b)**, the Combination 1 is more suitable for joints with a small total sheet thickness. Joints with a too large total sheet thickness could not be successfully connected due to undesired interlock values as presented in **Fig. 24(a)**. In contrast, as shown in **Fig. 24(d)**, the Combination 2 is more suitable for joints with a large total sheet thickness. Joints with a too small total sheet thickness could not be properly jointed because of the unsatisfied remaining bottom sheet thickness around the rivet tip, as presented in **Fig. 24(c)**. From the suitable application ranges (i.e. green regions) shown in **Fig. 24(b)(d)**, it was also noticed that the two rivet and die combinations are capable of connecting the majority of sheet combinations within the selected sheet thickness range $1.0\text{mm}\sim 2.0\text{mm}$.

With these application range maps, it is very convenient and straightforward for engineers, even inexperienced engineers, to identify whether or not a new sheet combination can be successfully connected by the selected rivet and die combination. Taking the sheet combinations $1.5\text{mm}+1.0\text{mm}$, $1.5\text{mm}+1.5\text{mm}$, $1.5\text{mm}+2.0\text{mm}$ as examples, the way to use the above two application range maps in practical applications was demonstrated. After locating the positions of the three sheet combinations on the application range maps shown in **Fig. 24(b)(d)**, it became very clear that the $1.5\text{mm}+1.0\text{mm}$ sheet combination cannot be successfully connected by either of the two rivet and die combinations. The $1.5\text{mm}+1.5\text{mm}$ sheet combination could only be successfully jointed by the rivet and die Combination 2. While the $1.5\text{mm}+2.0\text{mm}$ sheet combination could be connected by both of the two rivet and die combinations. These prediction results agreed well with the experimental tests, as listed in **Table 8**. Only the joint E-10 was not properly predicted because the tested interlock value (0.42mm) was too close to the quality threshold of interlock (0.4mm).

Different from the rivet and die selection approach proposed with GA, the application range map, once obtained, can be directly used to guide the selection of rivet and die without the need of running the ANNs

again. It is also a reliable tool to ensure that the workable rivet and die for a new sheet combination are selected from the accessible/existing rivets and dies. Such capability can potentially reduce the number of rivet and die combinations used in an automated assembly line, and thus is very valuable for practical applications. A practical application could be the design of a new vehicle and layout of a manufacturing line with SPR as the major joining technique.

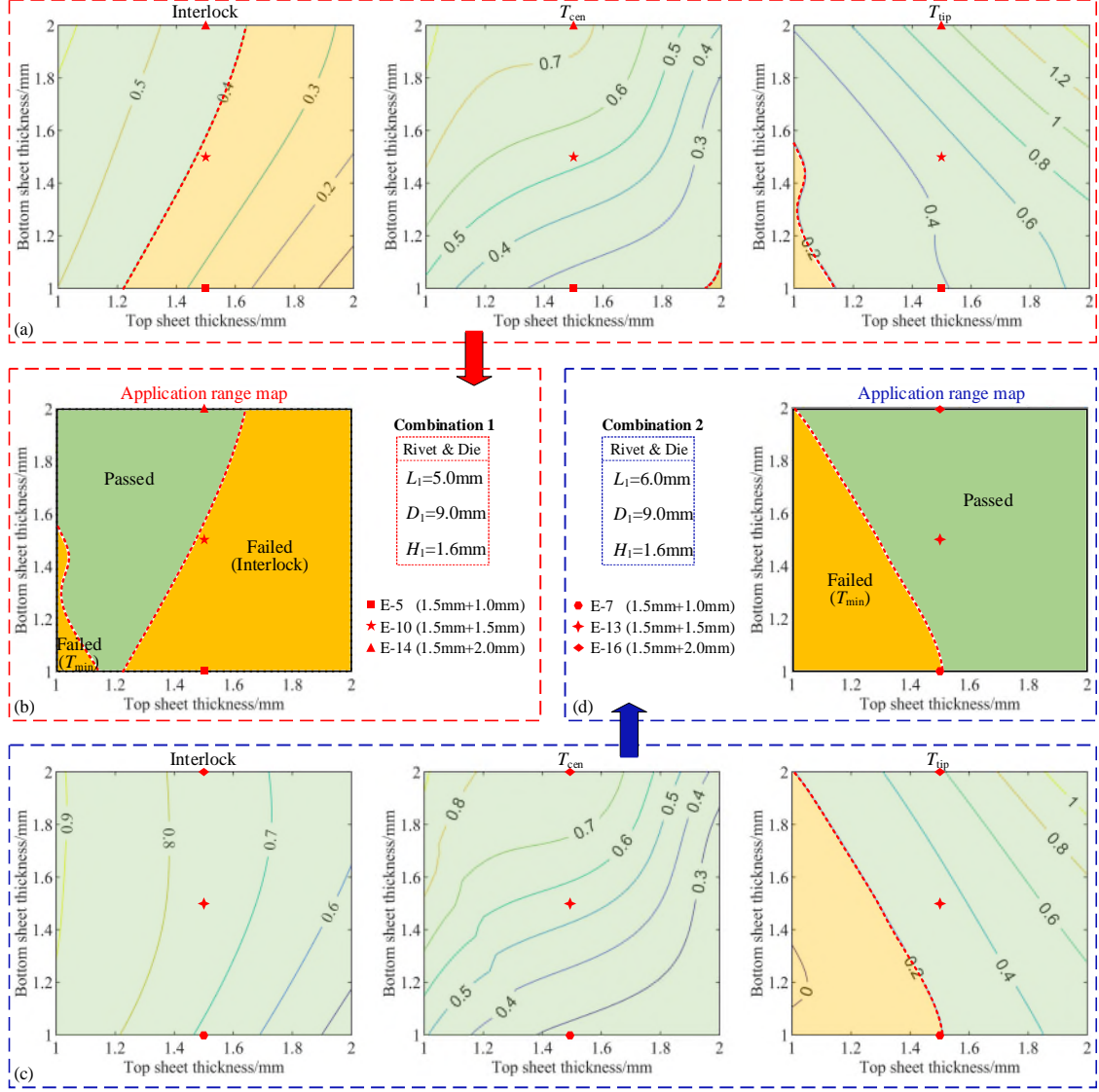


Fig. 24 Comparisons between application range maps of two rivet and die combinations (Quality standard: Interlock > 0.4mm & $T_{min} > 0.2\text{mm}$)

Table 8 Quality evaluation results with different rivet and die combinations

Joint configurations					Experimental results				Predicted (ANN)
Joint no.	Stack /mm (AA5754)	Rivet length L_1 /mm	Die		Rivet head height /mm (Mean)	Interlock /mm (Mean)	T_{min} /mm (Mean)	Passed /Failed	Passed /Failed
			Diameter D_1 /mm	Depth H_1 /mm					
E-5	1.5+1.0	5.0	9.0	1.6	-0.08	0.31	0.23	Failed	Failed
E-7	1.5+1.0	6.0	9.0	1.6	-0.08	0.74	0.1	Failed	Failed
E-10	1.5+1.5	5.0	9.0	1.6	0.02	0.42	0.53	Passed	Failed
E-13	1.5+1.5	6.0	9.0	1.6	0.01	0.77	0.41	Passed	Passed
E-14	1.5+2.0	5.0	9.0	1.6	-0.06	0.56	0.72	Passed	Passed
E-16	1.5+2.0	6.0	9.0	1.6	-0.12	0.93	0.43	Passed	Passed

6 Interaction analysis of joining parameters on joint quality

Another useful application of the developed ANNs is to analyze the interaction effects between different joining parameters on the joint quality. **Fig. 25** shows the interaction plots of the five joining parameters (i.e. T_1 , T_2 , L_1 , D_1 and H_1) on the interlock, T_{cen} and T_{tip} . The almost parallel trend lines suggest weak interactions, while the non-parallel trend lines indicate significant interactions between these parameters. Under the studied joint configurations, significant interaction effects on the interlock were observed between the D_1 and any of the other three parameters (T_2 , L_1 and H_1) as shown in **Fig. 25(a)**. While only the T_1 and T_2 demonstrated apparent interaction effects on the T_{cen} and T_{tip} as shown in **Fig. 25(b)(c)**. Therefore, the corresponding five contour graphs of the interlock, T_{cen} and T_{tip} were plotted with the ANNs, and discussed in the following sections.

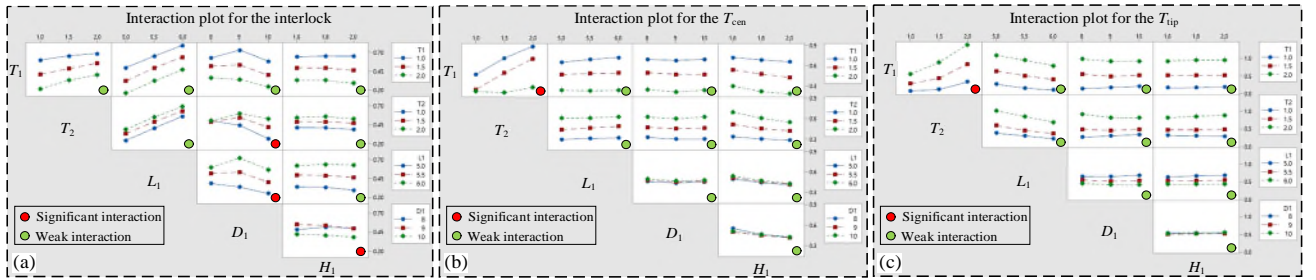


Fig. 25 Interaction plots of the five joining parameters on (a) the interlock, (b) the T_{cen} and (c) the T_{tip}

6.1 Interaction effects on the interlock

6.1.1 Between the bottom sheet thickness (T_2) and die diameter (D_1)

When the T_1 , L_1 and H_1 were fixed at 1.2mm, 5.0mm and 2.0mm, the contour graph of the interlock with varying T_2 and D_1 is plotted in **Fig. 26**. The non-parallel contour lines indicated the apparent interaction effects between the T_2 and D_1 on the interlock. It can be seen that the interlock always increased with the increment of the T_2 . A greater increasing speed of the interlock was found with a larger D_1 . In contrast, the interlock always decreased with the increment of the D_1 . A greater decreasing speed of the interlock was found with a smaller T_2 . To confirm such interaction effects, the cross-sectional profiles of joints corresponding to the points a ~ i were obtained from experimental SPR tests and FEA simulations, as shown in **Fig. 27**. Six of the nine joints were made experimentally due to the availability of dies. It can be seen that not only the changing trends but also the magnitudes of interlock matched well between **Fig. 26** and **Fig. 27**.

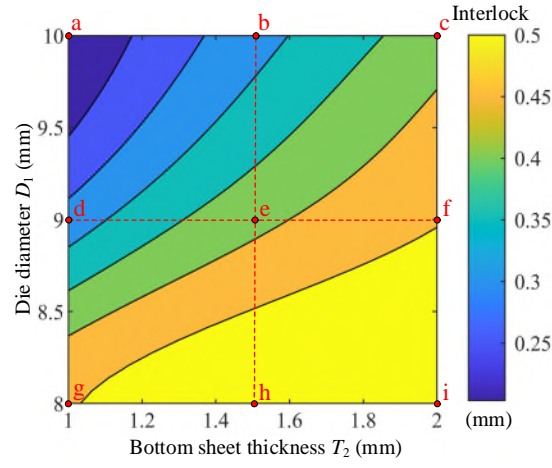


Fig. 26 Contour graph of the interlock with varying bottom sheet thickness T_2 and die diameter D_1 ($T_1=1.2\text{mm}$, $L_1=5.0\text{mm}$, $H_1=2.0\text{mm}$)

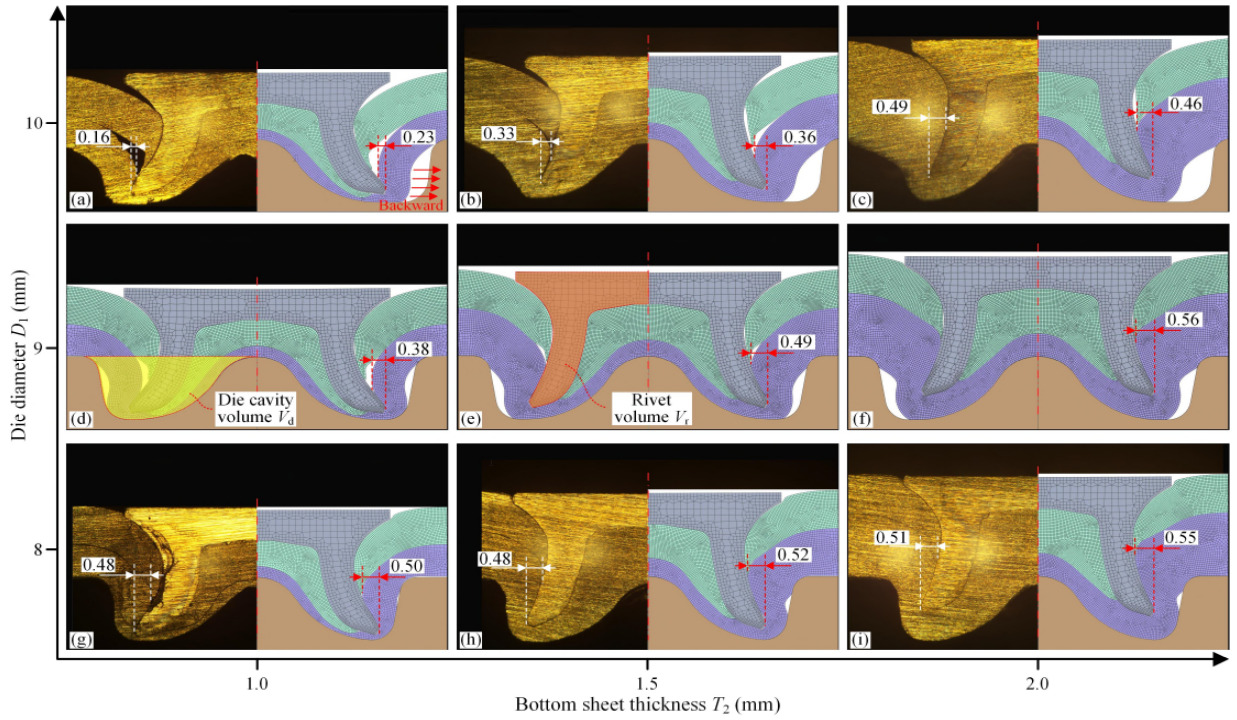


Fig. 27 Joint cross-sectional profiles with varying bottom sheet thickness T_2 and die diameter D_1 ($T_1=1.2\text{mm}$, $L_1=5.0\text{mm}$, $H_1=2.0\text{mm}$)

By analyzing the gradients of contour lines in **Fig. 26**, it can be seen that the interlock demonstrated a higher sensitivity to the T_2 with a large die diameter (e.g. 10.0mm at the points a to c) than with a small one (e.g. 8.0mm at the points g to i). This is mainly attributed to the different bottom sheet rigidities and the relative magnitudes of the rivet volume (V_r) and die cavity volume (V_d) shown in **Fig. 27(d)(e)**. When the D_1 was 10.0mm, the V_d (142.84mm^3) was much greater than the V_r (90.0mm^3). Due to the large unfilled die cavity space, the 1.0mm bottom sheet with a low rigidity was pressed backward rather than pierced by the rivet shank as shown in **Fig. 27(a)**. While as shown in **Fig. 27(c)**, the 2.0mm bottom sheet with a sufficient rigidity effectively prevented too much backward movement, and therefore allowed the rivet shank to flare deeply into the bottom sheet. So, the tested interlock rapidly increased from only 0.16mm to 0.49mm with the increment of the T_2 . In contrast, when the D_1 was 8.0mm, the V_d (89.07mm^3) almost equaled to the V_r (90.0mm^3). The small die diameter effectively limited the large movement of the bottom sheets, especially the 1.0mm one in

Fig. 27(g). Almost the same backward movements of the bottom sheets were observed as presented in **Fig. 27(g)(h)(i)**, and the rivet shank deeply flared into the bottom sheet in all of the three joints. Thus, the tested interlock just slightly increased from 0.48mm to 0.51mm with the increment of the T_2 .

In addition, the different gradients of contour lines also suggested that the interlock was more sensitive to the D_1 in SPR joints with a thin bottom sheet (e.g. 1.0mm at the points g to a) than with a thick one (e.g. 2.0mm at the points i to c). This phenomenon is also caused by the combined effects of the bottom sheet rigidity and the differentiation between the rivet and die volumes, and hence not discussed in detail.

6.1.2 Between the rivet length (L_1) and die diameter (D_1)

When the T_1 , T_2 and H_1 were fixed at 1.2mm, 1.8mm and 2.0mm, the contour graph of the interlock with varying L_1 and D_1 is shown in **Fig. 28(a)**. The non-parallel contour lines indicated the apparent interaction effects between the L_1 and D_1 on the interlock. With the different D_1 , the interlock always showed an increasing trend when the L_1 increased from 5.0mm to 6.0mm. Meanwhile, a slightly larger increment speed of the interlock was discovered with the $D_1=10.0$ mm than with the $D_1=8.0$ mm. In contrast, with the different L_1 , the changing trends of the interlock varied when the D_1 increased from 8.0mm to 10.0mm. For example, the interlock demonstrated a decreasing trend with the 5.0mm long rivets, but first increased and then decreased with the 6.0mm long rivets. **Fig. 29** shows the cross-sectional profiles of joints corresponding to the points a~i from experimental tests and FEA simulations. Among the nine profiles, four of them were experimentally obtained using the accessible dies. By comparing the **Fig. 28(a)** and **Fig. 29**, it can be seen that, although the interlock value at the point i was underestimated by the ANN, the predicted changing trends of the interlock from the ANN still showed reasonable agreements with that from both of the experimental tests and FEA simulations.

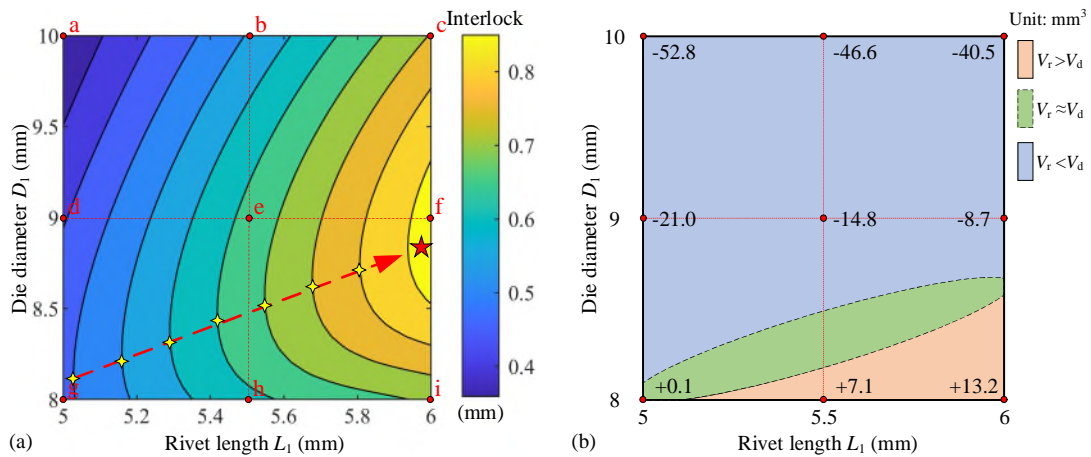


Fig. 28 Contour graphs of (a) the interlock and (b) the $V_r - V_d$ with varying rivet length L_1 and die diameter D_1 ($T_1=1.2$ mm, $T_2=1.8$ mm, $H_1=2.0$ mm)

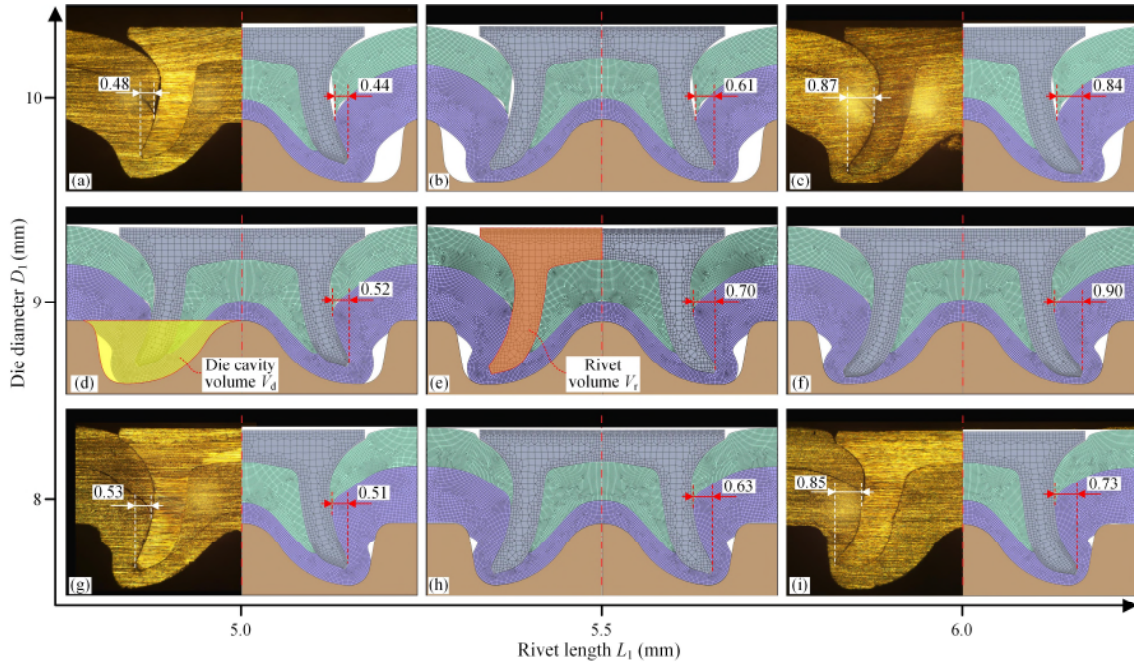


Fig. 29 Joint cross-sectional profiles with different rivet length L_1 and die diameter D_1 ($T_1=1.2\text{mm}$, $T_2=1.8\text{mm}$, $H_1=2.0\text{mm}$)

The interaction effect between the D_1 and L_1 on the interlock is also highly associated with the relative magnitudes of the V_r and V_d . **Fig. 28(b)** illustrates the contour graph of the difference ($V_r - V_d$) between the rivet and die cavity volumes with varying D_1 and L_1 . With the 8.0mm die diameter, the V_r of the 5.0mm long rivet (90.0mm^3) almost equaled to the V_d (89.07mm^3). Further increment of the L_1 led to a greater V_r than the V_d . The rivet shank underwent a high pressure after the die cavity was fully filled, and therefore was inevitably buckled as shown in **Fig. 29(i)**. At the same time, the relatively small die diameter ($D_1=8.0\text{mm}$) also limited the rivet shank flare. In contrast, with the 10.0mm die diameter, the V_r was always smaller than the V_d (142.84mm^3) as shown in **Fig. 28(b)**. The 1.8mm bottom sheet was rigid enough to prevent large backward movements, and the rivet shank still flared effectively into the bottom sheet, as shown in **Fig. 29(a)(b)(c)**. As a result, with the increment of the L_1 from 5.0mm to 6.0mm, the interlock showed a larger increasing speed with the 10.0mm die diameter than with the 8.0mm one. Similarly, when the D_1 increased from 8.0mm to 10.0mm, the different interlock changing patterns with varying L_1 can also be explained by the changes of the rivet shank flare and buckling degrees induced by the different volumes between the rivet and die. To avoid repetition, detailed discussions about this part are omitted.

The contour graph not only demonstrated the interaction effects but also visualized the maximum interlocks with possible optimal rivet and die combinations under the pre-defined conditions. For example, the yellow stars marked in **Fig. 28(a)** presented the maximum interlocks with the optimal D_1 for different length rivets. From the positions of these yellow stars, it can be seen that the optimal D_1 slightly increased with the increment of L_1 , and the maximum interlock occurred (i.e. red star) when the L_1 reached its maximum value 6.0mm. Due to such strong interactions between the L_1 and D_1 , the influences of the L_1 and D_1 on the interlock should be considered simultaneously.

6.1.3 Between the die diameter (D_1) and die depth (H_1)

When the T_1 , T_2 and L_1 were fixed at 1.2mm, 1.8mm and 5.0mm, the contour graph of the interlock with

varying D_1 and H_1 is shown in **Fig. 30(a)**. The non-parallel contour lines confirmed the apparent interaction effects between the D_1 and H_1 on the interlock. It can be seen that the changing trend of the interlock varied with the changes of the D_1 and H_1 . For example, when the D_1 increased from 8.0mm to 10.0mm, the interlock first increased and then decreased with the $H_1=1.6$ mm, while it demonstrated a decline trend with the $H_1=2.0$ mm. Similarly, when the H_1 increased from 1.6mm to 2.0mm, the interlock also demonstrated different variation trends with the $D_1=8.0$ mm and $D_1=10.0$ mm. The cross-sectional profiles of joints corresponding to the points a~i obtained from the experimental tests and FEA simulations are presented in **Fig. 31**. Four of the nine joints were made experimentally using the accessible dies. By comparing the contour graph with the joint cross-sectional profiles, it can be concluded that the predicted changing trends of the interlock from the ANN showed a reasonable agreement with that from both of the experimental SPR test and FEA simulation.

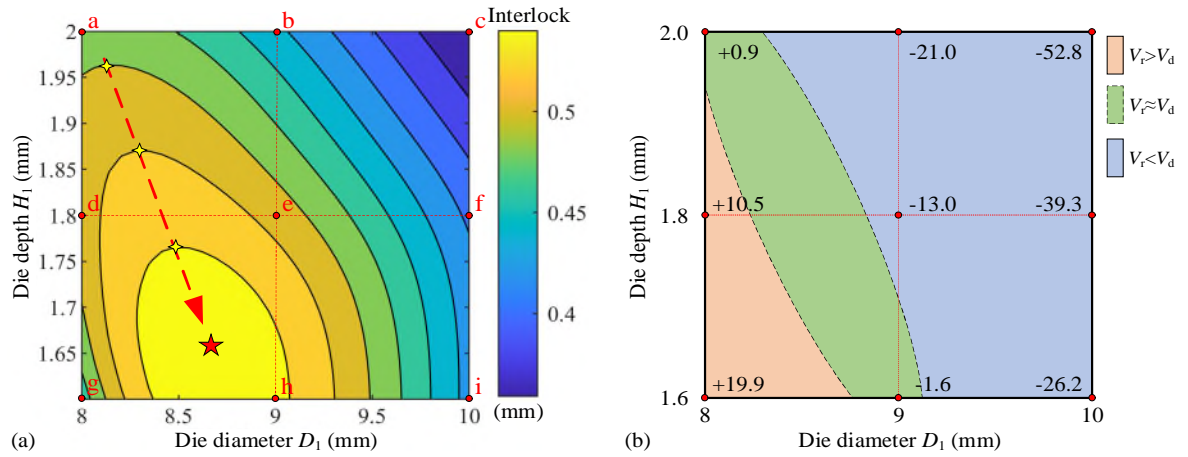


Fig. 30 Contour graphs of (a) the interlock and (b) the $V_r - V_d$ with varying die diameter D_1 and die depth H_1 ($T_1=1.2$ mm, $T_2=1.8$ mm, $L_1=5.0$ mm)

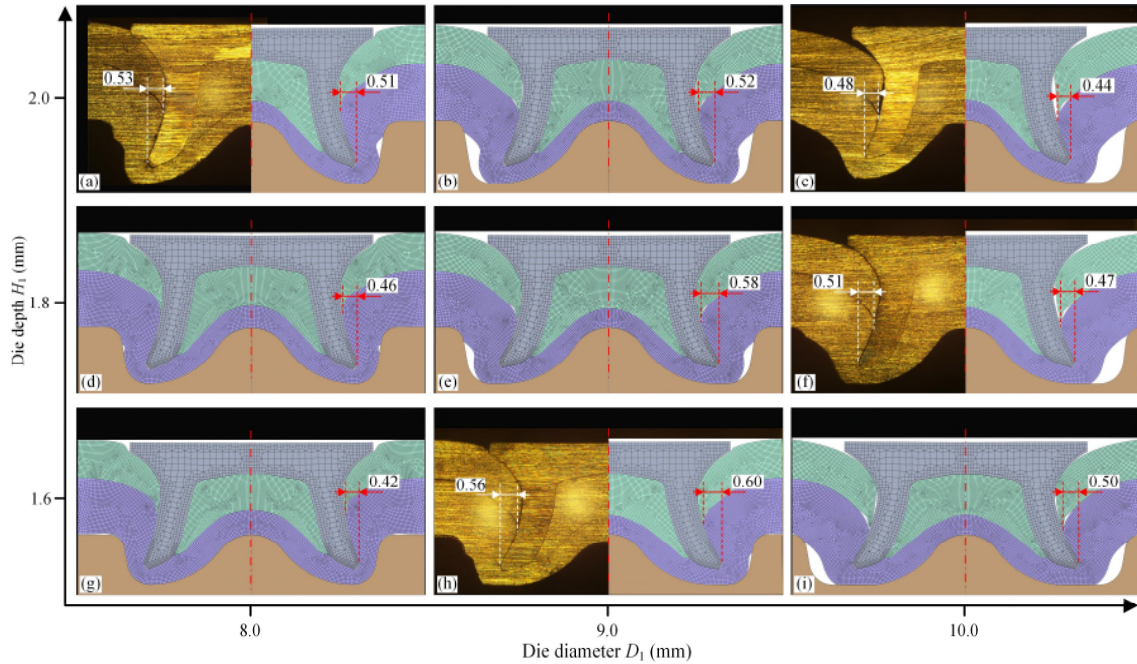


Fig. 31 Joint cross-sectional profiles with different die diameter D_1 and die depth H_1 ($T_1=1.2$ mm, $T_2=1.8$ mm, $L_1=5.0$ mm)

The interaction effects between the D_1 and H_1 on the interlock are also highly associated with the relative magnitude of the V_r and V_d . **Fig. 30(b)** illustrates the contour graph of the difference between the V_r and V_d

with varying D_1 and H_1 . As mentioned above, if the V_d is smaller than the V_r , it would be very difficult for the rivet shank to further flare into the bottom sheet after the die cavity is fully filled. Instead, the rivet shank buckling happens and imposes negative influences on the interlock formation. On the other hand, if the V_d is greater than the V_r , the bottom sheet would undergo a large displacement towards the die cavity and thus could not be effectively pierced by the rivet shank. This would also impose a negative influence on the interlock formation. The increment of the H_1 from the points g to a effectively increased the V_d as shown in **Fig. 30(b)**. This provides enough volume for the rivet shank to flare, but not too much for the bottom sheet to deform freely into the die cavity. As a result, the rivet shank buckling degree was effectively reduced as shown in **Fig. 31(g)(d)(a)**, which led to the increasing trend of the interlock with the 8.0mm die diameter. In contrast, from the points h to b and from the points i to c, the increment of the H_1 led to an increasingly larger V_d compared with the V_r as shown in **Fig. 30(b)**. As a result, the interlock showed decreasing tendencies with the 9.0mm and 10.0mm die diameters. The same principles can also be applied to explain the different changing trends of interlock when the D_1 increased from 8.0mm to 10.0mm. As shown in **Fig. 30(a)**, when the $H_1=1.6$ mm, the interlock first increased due to the reduction of rivet shank bulking degree and then decreased because of the increasingly larger backward movement of the bottom sheet. While when the $H_1=2.0$ mm, the interlock showed a decreasing trend because the V_d became increasingly larger than the V_r .

Similar to the previous section, the contour graph also visualized the maximum interlocks with possible optimal combinations of the D_1 and H_1 under the pre-defined conditions. For example, the yellow stars marked in **Fig. 30(a)** presented the maximum interlocks with the optimal D_1 for different H_1 . From the positions of these yellow stars, it can be seen that the optimal D_1 slightly increased with the decrease of H_1 , and the maximum interlock occurred (i.e. red star) when the H_1 reached around 1.65mm. By observing the relative rivet and die volumes on **Fig. 30(b)** corresponding to the locations of these yellow stars on **Fig. 30(a)**, the importance of choosing similar rivet and die volumes to maximize the interlock for a SPR joint was highlighted.

6.2 Interaction effects on the T_{cen} and T_{tip}

As mentioned above, strong interaction effects on the T_{cen} and T_{tip} were only discovered between the T_1 and T_2 . When the L_1 , D_1 and H_1 were fixed at 5.0mm, 10.0mm, 1.8mm, the contour graph of the T_{cen} with varying T_1 and T_2 is shown in **Fig. 32(a)**. The apparent interaction effects between the T_1 and T_2 on the T_{cen} were highlighted by the non-parallel contour lines. The tested and FEA simulated cross-sectional profiles of joints corresponding to the points a ~ i are shown in **Fig. 33**. Five of the nine joints were made experimentally due to the availability of dies. It can be seen that the predicted changing trends of the T_{cen} from the ANN showed a reasonable agreement with that from the experimental SPR tests and the FEA simulations. With the different T_2 , the T_{cen} always decreased when the T_1 increased from 1.2mm to 1.8mm. A slightly greater decreasing speed of T_{cen} was captured with a larger T_2 . The decline of the T_{cen} is because the thicker top sheet takes a longer time to be penetrated by the rivet shank [9], while the greater speed of the T_{cen} might be mainly attributed to the relatively higher rigidity of the thicker bottom sheet. In contrast, with the different T_1 , the T_{cen} always increased when the T_2 changed from 1.2mm to 1.8mm. A larger increasing speed of T_{cen} was found with a smaller T_1 . The increment of the T_{cen} is directly linked with the increment of the initial bottom sheet thickness at the joint center, while the larger speed of the T_{cen} might be attributed to the relatively lower pressure applied around the

center of the bottom sheet by the thinner top sheet. The largest T_{cen} was captured on the top left corner while the smallest value was observed on the lower right corner of the contour graph.

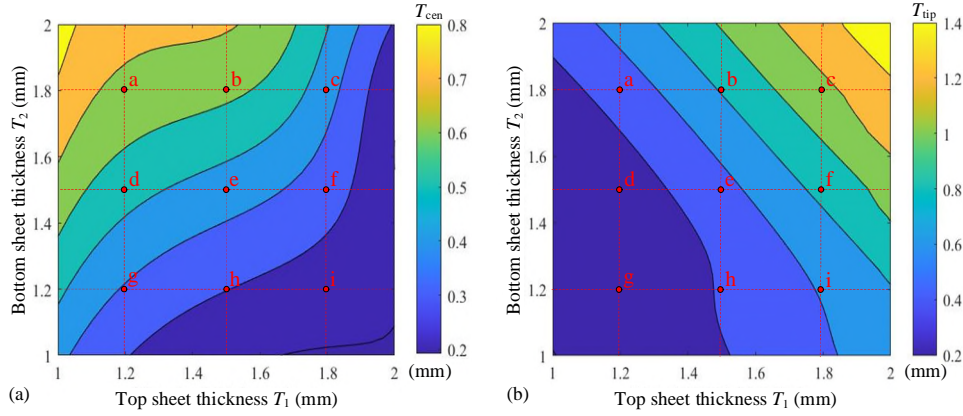


Fig. 32 Contour graph of the (a) T_{cen} and (b) T_{tip} with varying top and bottom sheet thicknesses ($L_1=5.0\text{mm}$, $D_1=10.0\text{mm}$, $H_1=1.8\text{mm}$)

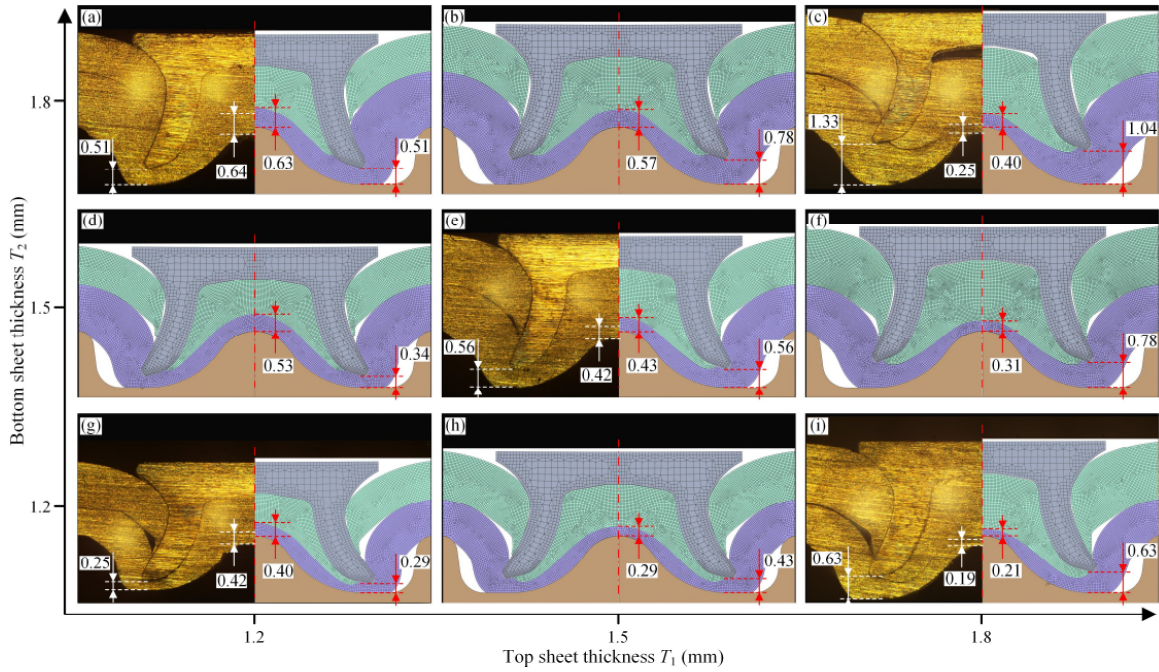


Fig. 33 Joint cross-sectional profiles with varying top and bottom sheet thicknesses ($L_1=5.0\text{mm}$, $D_1=10.0\text{mm}$, $H_1=1.8\text{mm}$)

When the L_1 , D_1 and H_1 were fixed at 5.0mm, 10.0mm, 1.8mm, the contour graph of the T_{tip} with varying T_1 and T_2 is shown in **Fig. 32(b)**. The non-parallel contour lines demonstrated the interaction effects between the T_1 and T_2 on the T_{tip} . The predicted changing trends of the T_{tip} from the ANN in **Fig. 32(b)** showed a reasonable agreement with that from the experimental SPR tests and the FEA simulations in **Fig. 33**. It can be seen that the T_{tip} always showed an increasing trend with the increments of the T_1 and T_2 . This is because the increment of the T_1 or T_2 increased the total sheet thickness and led to a larger distance between the final position of the rivet tip and the bottom of the die cavity. When the T_2 increased from 1.2mm to 1.8mm, a larger increasing speed of T_{tip} was found with a thicker top sheet. Similarly, when the T_1 changed from 1.2mm to 1.8mm, a larger increment speed of T_{tip} was also observed with a thicker bottom sheet. This phenomenon is attributed to the different impact degrees of the sheet thickness changes on the rivet shank flare. For instance, **Fig. 34** shows the rivet shank deformations from points a to c with $T_2=1.8\text{mm}$ and from the points g to i with $T_2=1.2\text{mm}$. An

apparent increase of the deformed rivet length along the vertical direction was found from points g to i due to the smaller rivet shank flare. While the deformed rivet length along the vertical direction kept almost constant from the points a to c. The increment of the deformed rivet length directly led to a smaller T_{tip} . Thus, with the increment of the T_1 , a larger increment speed of T_{tip} was observed with a thicker bottom sheet. Different from the T_{cen} , the largest T_{tip} was found on the top right corner while the smallest value was observed on the lower left corner of the contour graph.

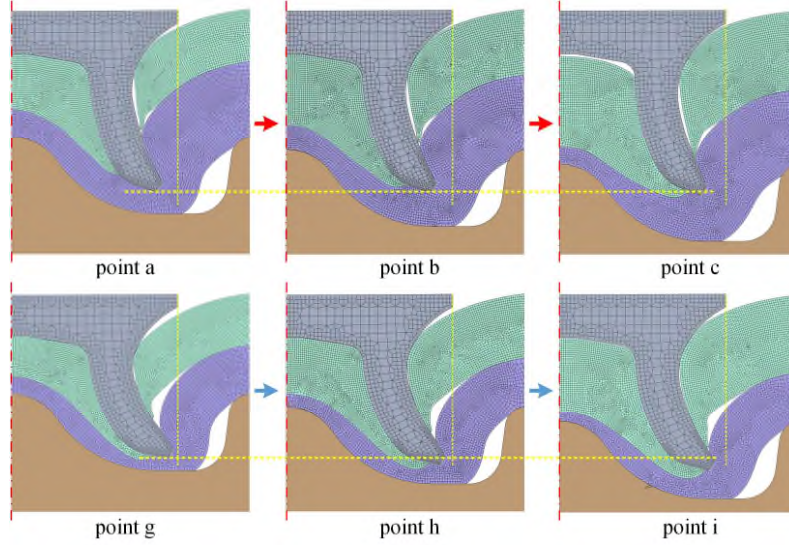


Fig. 34 Deformed rivet shank in SPR joints with different top and bottom sheet thicknesses

7 Conclusions

In this study, artificial neural network (ANN) models involving five critical joining parameters were developed to predict the SPR joint quality. Two innovative approaches were also proposed to simplify and optimize the selection of rivet and die for new sheet combinations. In addition, the interaction effects between five joining parameters on the joint quality indicators were also discussed with the contour graphs plotted by the developed ANNs. The main conclusions are summarized below:

- (1) Three ANN models for the interlock, T_{cen} and T_{tip} were established respectively for prediction of the SPR joint quality. The varying optimal ANN structures suggested that developing an individual ANN model for each quality indicator could maximize the prediction accuracy. The verified FEA model of SPR process can be used to collect training and testing data for ANN model development.
- (2) The accuracy of developed ANNs was validated with experimental SPR tests. The MAE, MAPE and r for the interlock between the experimental SPR test and ANN were 0.058mm, 14.2% and 0.978 respectively. The corresponding MAE, MAPE and r for the T_{cen} were 0.075mm, 22.4% and 0.881. The MAE, MAPE and r for the T_{tip} were 0.059mm, 10.9% and 0.996 respectively.
- (3) The genetic algorithm (GA) combined with the developed ANNs can be used to simplify and optimize the selection of rivet and die for new sheet combinations. With the generated Pareto optimal solution set, the suitable rivet and die combinations can be easily selected to achieve the optimal joint quality according to different quality standards.

(4) Application range maps of different rivet and die combinations can be created with the help of the developed ANNs. In practical applications, these maps offer a simple but effective solution for the selection of suitable and accessible rivet and die for new sheet combinations. It also has great potential to be applied in the design of a new vehicle and layout of a manufacturing line with SPR as the major joining technique.

(5) The developed ANNs showed very good performances in the interaction analysis between different joining parameters. Under the studied joint configurations, significant interaction effects on the interlock were identified between the D_1 and any of the other three parameters (T_2 , L_1 and H_1), while only the T_1 and T_2 demonstrated apparent interaction effects on the T_{cen} and T_{tip} . The strong interaction effects on the three quality indicators were discovered to be highly associated with the relative magnitude of the rivet and die volumes, the rivet shank flare and the sheet rigidity.

CRedit authorship contribution statement

Huan Zhao: Methodology, Writing-original draft, Writing-review & editing, Investigation. **Li Han:** Supervision, Writing-review & editing. **Yunpeng Liu:** Methodology, Writing-review & editing, Investigation. **Xianping Liu:** Supervision, Project administration, Funding acquisition.

Declaration of competing interest

The authors declare that they have no known competing financial interests or personal relationships that could have appeared to influence the work reported in this paper.

Acknowledgements

This work was supported by Jaguar Land Rover. The authors would like to thank Dr. Matthias Wissling, Paul Bartig and their team members from Tucker GmbH for their supports during the laboratory tests.

References

- [1] Mori K, Abe Y, Kato T. Self-pierce riveting of multiple steel and aluminium alloy sheets. J Mater Process Technol 2014;214:2002–8. <https://doi.org/10.1016/j.jmatprotec.2013.09.007>.
- [2] Rusia A, Weihe S. Development of an end-to-end simulation process chain for prediction of self-piercing riveting joint geometry and strength. J Manuf Process 2020;57:519–32. <https://doi.org/10.1016/j.jmapro.2020.07.004>.
- [3] Li D, Chrysanthou A, Patel I, Williams G. Self-piercing riveting-a review. Int J Adv Manuf Technol 2017;92:1777–824. <https://doi.org/10.1007/s00170-017-0156-x>.
- [4] Karim MA, Jeong TE, Noh W, Park KY, Kam DH, Kim C, et al. Joint quality of self-piercing riveting

(SPR) and mechanical behavior under the frictional effect of various rivet coatings. *J Manuf Process* 2020;58:466–77. <https://doi.org/10.1016/j.jmapro.2020.08.038>.

- [5] Hoang NH, Porcaro R, Langseth M, Hanssen AG. Self-piercing riveting connections using aluminium rivets. *Int J Solids Struct* 2010;47:427–39. <https://doi.org/10.1016/j.ijsolstr.2009.10.009>.
- [6] Uhe B, Kuball CM, Merklein M, Meschut G. Improvement of a rivet geometry for the self-piercing riveting of high-strength steel and multi-material joints. *Prod Eng* 2020. <https://doi.org/10.1007/s11740-020-00973-w>.
- [7] Kraus C, Falk T, Mauermann R, Drossel W-G. Development of a New Self-flaring Rivet Geometry Using Finite Element Method and Design of Experiments. *Procedia Manuf* 2020;47:383–8. <https://doi.org/10.1016/J.PROMFG.2020.04.295>.
- [8] Deng JH, Lyu F, Chen RM, Fan ZS. Influence of die geometry on self-piercing riveting of aluminum alloy AA6061-T6 to mild steel SPFC340 sheets. *Adv Manuf* 2019;7. <https://doi.org/10.1007/s40436-019-00250-9>.
- [9] Liu Y, Li H, Zhao H, Liu X. Effects of the die parameters on the self-piercing riveting process. *Int J Adv Manuf Technol* 2019;105:1–16. <https://doi.org/10.1007/s00170-019-04567-4>.
- [10] Abe Y, Kato T, Mori K. Self-piercing riveting of high tensile strength steel and aluminium alloy sheets using conventional rivet and die. *J Mater Process Technol* 2009;209:3914–22. <https://doi.org/10.1016/J.JMATPROTEC.2008.09.007>.
- [11] Ma YW, Lou M, Li YB, Lin ZQ. Effect of rivet and die on self-piercing rivetability of AA6061-T6 and mild steel CR4 of different gauges. *J Mater Process Technol* 2018;251:282–94. <https://doi.org/10.1016/j.jmatprotec.2017.08.020>.
- [12] Mucha J. A study of quality parameters and behaviour of self-piercing riveted aluminium sheets with different joining conditions. *Stroj Vestnik/Journal Mech Eng* 2011;57:323–33. <https://doi.org/10.5545/sv-jme.2009.043>.
- [13] Carandente M, Dashwood RJ, Masters IG, Han L. Improvements in numerical simulation of the SPR process using a thermo-mechanical finite element analysis. *J Mater Process Technol* 2016;236:148–61. <https://doi.org/10.1016/J.JMATPROTEC.2016.05.001>.
- [14] Atzeni E, Ippolito R, Settineri L. FEM Modeling of Self-Piercing Riveted Joint. *Key Eng Mater* 2007;344:655–62. <https://doi.org/10.4028/www.scientific.net/KEM.344.655>.
- [15] Chen C, Zhao S, Han X, Cui M, Fan S. Optimization of a reshaping rivet to reduce the protrusion height and increase the strength of clinched joints. *J Mater Process Technol* 2016;234:1–9. <https://doi.org/10.1016/j.jmatprotec.2016.03.006>.
- [16] Zhao H, Han L, Liu Y, Liu X. Modelling and interaction analysis of the self-pierce riveting process using regression analysis and FEA. *Int J Adv Manuf Technol* 2021:1–18. <https://doi.org/10.1007/s00170-020-06519-9>.

- [17] Zhang YH, Shi BJ, Zhong JB. Multi-parameter joint optimization of self-piercing riveting on aluminum alloy plate. *J. Phys. Conf. Ser.*, vol. 1605, 2020. <https://doi.org/10.1088/1742-6596/1605/1/012093>.
- [18] Tassler T, Israel M, Goede MF, Dilger K, Dröder K. Robust joining point design for semi-tubular self-piercing rivets. *Int J Adv Manuf Technol* 2018;98:431–40. <https://doi.org/10.1007/s00170-018-2238-9>.
- [19] Paliwal M, Kumar UA. Neural networks and statistical techniques: A review of applications. *Expert Syst Appl* 2009;36:2–17. <https://doi.org/10.1016/j.eswa.2007.10.005>.
- [20] Lambiase F, Grossi V, Paoletti A. Machine learning applied for process design of hybrid metal-polymer joints. *J Manuf Process* 2020;58:92–100. <https://doi.org/10.1016/J.JMAPRO.2020.08.016>.
- [21] Fang Y, Huang L, Zhan Z, Huang S, Han W. Effect Analysis for the Uncertain Parameters on Self-Piercing Riveting Simulation Model Using Machine Learning Model. *SAE Tech Pap* 2020;2020-April. <https://doi.org/10.4271/2020-01-0219>.
- [22] Khorasani AM, Gibson I, Ghasemi AH, Ghaderi A. Modelling of laser powder bed fusion process and analysing the effective parameters on surface characteristics of Ti-6Al-4V. *Int J Mech Sci* 2020;168:105299. <https://doi.org/10.1016/j.ijmecsci.2019.105299>.
- [23] Wang H, Zhang Z, Liu L. Prediction and fitting of weld morphology of Al alloy-CFRP welding-rivet hybrid bonding joint based on GA-BP neural network. *J Manuf Process* 2020;1–12. <https://doi.org/10.1016/j.jmapro.2020.04.010>.
- [24] Liu J, Zhao Z, Bi Y, Dong H. Prediction and compensation of force-induced deformation for a dual-machine-based riveting system using FEM and neural network. *Int J Adv Manuf Technol* 2019;103:3853–70. <https://doi.org/10.1007/s00170-019-03826-8>.
- [25] Katoch S, Chauhan SS, Kumar V. A review on genetic algorithm: past, present, and future. *Multimedia Tools and Applications*; 2020. <https://doi.org/10.1007/s11042-020-10139-6>.
- [26] Wang Y, Yu J, Song Y, Chen F. Parameter optimization of the composite honeycomb tip in a turbine cascade. *Energy* 2020;197:117236. <https://doi.org/10.1016/j.energy.2020.117236>.
- [27] Udayakumar T, Raja K, Afsal Husain TM, Sathiya P. Prediction and optimization of friction welding parameters for super duplex stainless steel (UNS S32760) joints. *Mater Des* 2014;53:226–35. <https://doi.org/10.1016/j.matdes.2013.07.002>.
- [28] Zhang B, Chen X, Pan K, Wang J. Multi-objective optimization of friction stir spot-welded parameters on aluminum alloy sheets based on automotive joint loads. *Metals (Basel)* 2019;9. <https://doi.org/10.3390/met9050520>.
- [29] Han L, Chrysanthou A. Evaluation of quality and behaviour of self-piercing riveted aluminium to high strength low alloy sheets with different surface coatings. *Mater Des* 2008;29:458–68. <https://doi.org/10.1016/j.matdes.2006.12.020>.
- [30] Haque R. Quality of self-piercing riveting (SPR) joints from cross-sectional perspective: A review.

- [31] Liu Y, Han L, Zhao H, Liu X. Evaluation and correction of cutting position's effects on quality indicator measurement of self-piercing riveted joint. Mater Des 2021;109583. <https://doi.org/10.1016/J.MATDES.2021.109583>.
- [32] Han L, Thornton M, Li D, Shergold M. Effect of setting velocity on self-piercing riveting process and joint behaviour for automotive applications. SAE Tech Pap 2010. <https://doi.org/10.4271/2010-01-0966>.
- [33] Kam DH, Jeong TE, Kim MG, Shin J. Self-piercing riveted joint of vibration-damping steel and aluminum alloy. Appl Sci 2019;9. <https://doi.org/10.3390/app9214575>.
- [34] Xu B, Zhang H, Wang Z, Wang H, Zhang Y. Model and Algorithm of BP Neural Network Based on Expanded Multichain Quantum Optimization. Math Probl Eng 2015;2015. <https://doi.org/10.1155/2015/362150>.
- [35] Olden JD, Joy MK, Death RG. An accurate comparison of methods for quantifying variable importance in artificial neural networks using simulated data. Ecol Modell 2004;178:389–97. <https://doi.org/10.1016/j.ecolmodel.2004.03.013>.
- [36] Deb K. Multi-Objective Optimization Using Evolutionary Algorithms: An introduction. Multi-Objective Optim. using Evol. Algorithms, 2001. <https://doi.org/10.1001/jama.1943.02840160014004>.